Angiogenesis and vessel co-option in a mathematical model of diffusive tumor growth: The role of chemotaxis ☆

A. Gandolfi [f,†], S.De Franciscis [a], A. d'Onofrio [b,c], A. Fasano [d,e,f,*], C. Sinisgalli [f]

[a] *Instituto de Astrofísica de Andalucía (IAA-CSIC), Granada, Spain*
[b] *International Prevention Research Institute, Lyon, France*
[c] *Department of Mathematics and Statistics, Strathclyde University, Glasgow, Scotland, United Kingdom*
[d] *Dipartimento di Matematica "U. Dini", Università di Firenze, Florence, Italy*
[e] *FIAB SpA, Vicchio (Florence), Italy*
[f] *Istituto di Analisi dei Sistemi ed Informatica "A. Ruberti" – CNR, Rome, Italy*

ARTICLE INFO

Article history:
Accepted 14 October 2020

Keywords:
Modeling vascularized tumor growth
Angiogenesis
Chemotaxis
Tumor invasion
Traveling waves
Fickian diffusion

ABSTRACT

This work considers the propagation of a tumor from the stage of a small avascular sphere in a host tissue and the progressive onset of a tumor neovasculature stimulated by a pro-angiogenic factor secreted by hypoxic cells. The way new vessels are formed involves cell sprouting from pre-existing vessels and following a trail via a chemotactic mechanism (CM). Namely, it is first proposed a detailed general family of models of the CM, based on a statistical mechanics approach. The key hypothesis is that the CM is composed by two components: i) the well–known bias induced by the angiogenic factor gradient; ii) the presence of stochastic changes of the velocity direction, thus giving rise to a diffusive component. Then, some further assumptions and simplifications are applied in order to derive a specific model to be used in the simulations. The tumor progression is favored by its acidic aggression towards the healthy cells. The model includes the evolution of many biological and chemical species. Numerical simulations show the onset of a traveling wave eventually replacing the host tissue with a fully vascularized tumor. The results of simulations agree with experimental measures of the vasculature density in tumors, even in the case of particularly hypoxic tumors.

1. Introduction

The growth of solid tumors as avascular nodules cannot exceed the size of 1-2 mm of diameter since, beyond this size, the diffusion of solutes from the surrounding environment is insufficient to appropriately supply the cells with oxygen and nutrients, as shown by experiments on *in vitro* tumor cellular spheroids (Freyer and Sutherland, 1986). Indeed, the tumor needs to be vascularized to grow further.

Generally, tumor vascularization requires the development of new blood vessels following the proliferation of endothelial cells (ECs) of pre-existing vessels and the formation of sprouts. This kind of vascularization mechanism is called angiogenesis (Adair et al., 2010). The angiogenesis process is under the control of a complex interplay of chemical factors, both pro-angiogenic and anti-angiogenic, secreted by the tumor cells and the stromal cells. The process initiates with the activation into proliferation of the endothelial cells of pre-existing vessels that give origin to sprouts. Sprouts in turn proliferate creating a structure along the motion of the tip cell whose orientation is biased by the gradient of the angiogenic factor, subjected at the same time to a random change. After anastomosis and some maturation process, such structures form a network of new vessels allowing blood flow (Carmeliet et al., 2011).

Interest has been devoted over the past 40 years to the mathematical modeling of blood vessel formation with focus on the migratory response of endothelial cells to angiogenic factors since the works of Ausprunk et al. (1977); Zigmond, 1977. Theoretical studies on blood vessel growth and development may however be traced back nearly a century (see e.g. Mantzaris et al., 2004; Chaplain et al., 2006; Adair et al., 2010).

Much interest has been devoted to the mathematical modeling of tumor–induced angiogenesis (Hahnfeldt et al., 1999; d'Onofrio et al., 1999; d'Onofrio et al., 2009; d'Onofrio and Gandolfi, 2010) as well as to both anti–angiogenesis therapies (Hahnfeldt et al.,

☆ This article is dedicated to the memory of our dear friend and colleague Alberto Gandolfi who passed away just before the work was completed.

* Corresponding author at: Dipartimento di Matematica "U. Dini", Università di Firenze, Florence, Italy.
E-mail address: a.fasano@fiab.it (A. Fasano).

† Author passed away.

1999; d'Onofrio et al., 1999; d'Onofrio and Gandolfi, 2006; d'Onofrio et al., 2009; d'Onofrio et al., 2009) and the effects on tumor vessels of anticancer chemo- and radiotherapies (d'Onofrio and Gandolfi, 2010; Ledzewicz et al., 2012). As far as the spatio–temporal dynamics, a particular effort has been focused on continuum modeling of angiogenesis (Hillen and Painter, 2009), starting with the work of Balding and McElwain (1985) who describe the growth of a capillary network in terms of tip and sprout densities in response to angiogenic growth factors.

Furthermore, we mention discrete models of angiogenesis treating cells as individual units and incorporating cell movement and interaction with the tissue (Anderson and Chaplain, 1998; Rivero et al., 1989). Discrete models incorporating rules for sprout branching and anastomoses that include elements of stochasticity for the cell movement have also been proposed (see for instance Othmer et al., 1988; Tranquillo et al., 1988; Anderson and Chaplain, 1998).

Among the attempts of modeling tumor angiogenesis with attention to optimal treatment strategies we quote the very recent paper by Voutouri et al. (2019) in which the sprouting of new vessels is described by means of two endothelial cell populations, that the authors call "stable" and "unstable", respectively, both subject to a chemotactic motion simply governed by the gradient of angiogenic factors.

Our approach differs in various aspects from previous works. In particular we perform a finer analysis of chemotaxis, which includes a random component generated by tumbling of the unstable cells and is based on different principles (the sheer proportionality to the gradient of the chemotactic factor is known to be not always adequate - and actually is not in this specific case, where the gradient influences the orientation of velocity, but not its modulus). The concept pursued here is that the angiogenic factor gradient contributes to determine the tip cells orientation but not their speed intensity.

The aim of this work is to build a mathematical model to describe the growth of an invasive tumor within the host tissue from its initial (avascular) phase, elucidating the relative role of the neo-angiogenesis and of the possible vessel co-option, and performing numerical simulations. Particular attention is devoted to the stages giving rise to the new vasculature.

The model is formulated in Section 2. It includes the tumor aggression to the surrounding healthy tissue. Modeling the formation of new vessels within the tumor goes through the description of the evolution of different classes of cells under the stimulus of a protein secreted by hypoxic tumor cells. In particular, we derive a model for tip cell chemotactic migration under the influence of the angiogenic factor. The numerical approach is explained in Section 3. The values of the various parameter are listed and discussed in Section 4. Results are shown and commented in Section 5. Starting from a spherical, avascular tumor, simulations show that tumor progresses as a traveling wave, eventually replacing the health tissue. The paper contains two appendices. App. A shows that all the quantities involved in the model stay in their natural physical range; App. B analyzes the steady state created after the healthy tissue has been replaced by the tumor. The analytical results of App. B proved to be very useful in checking the validity of numerical simulation. Our numerical results agree with the available experimental data on tumor vasculature in a wide range of cases.

2. Model formulation

2.1. General assumptions

Both the tumor and the host tissue in which the tumor is developing are viewed as a mixture of cells of different types, vessels, interstitial liquids and extracellular matrix (ECM). We denote by $\phi(x,t)$ the local volume fraction occupied by cells and vessels at position x and time t, with $x \in \Omega \subset IR^3$. Ω is the domain on which the model is defined, and it has to be viewed as a small portion of the body. Under the saturation hypothesis, $1-\phi$ is the fraction occupied by fluids plus ECM. The extracellular matrix, which is a network of fibrillar protein and proteoglycans necessary to allow active cell motility, is produced by stromal cells and degraded through enzymes secreted by the tumor cells (Chaplain et al., 1993). In the present model, for simplicity, we disregard the ECM dynamics assuming that it is incompressible with constant volume fraction ϕ_{ECM}. Similarly, the dynamics of liquids is also disregarded, along with any mechanical interaction of cells with the surroundings. Likewise, the possible displacement of the vessel network caused by tumor growth is not accounted for. The evolution of the vessel network – including normal host vessels and neoformed vessels – will be traced by the dynamics of the involved populations of endothelial cells.

Furthermore, we assume that random and directed cell motility, as well as cell proliferation, decrease as the occupied volume fraction ϕ increases, and that cellular movement and proliferation cease when ϕ reaches some value ϕ^*. Obviously, ϕ^* cannot exceed the maximal volume fraction available for cells and vessels, and thus it must be $\phi^* \leqslant 1-\kappa\phi_{ECM}$, where the coefficient $\kappa > 1$ accounts for the steric hindrance that increases the space actually excluded by ECM.

Although the movement impairment in crowded environments and the inhibition of cell proliferation are likely to follow different laws with respect to ϕ, we describe for simplicity both these phenomena by means of a common function $B(\phi)$ that multiplicatively modifies the proliferation rates as well as the diffusion and chemotaxis terms. The function $B(\phi)$ is such that $B(0)=1, B(\phi^*)=0$, and $B'(\phi)<0$; in particular we take (see (Swanson et al., 2011))

$$B(\phi) = \left(1-\frac{\phi}{\phi^*}\right)^p, \qquad p>1. \tag{1}$$

2.2. Tumor cells and host tissue

We suppose that tumor cells are endowed with active random motility, which can be described by moderate Fickian diffusion. Tumor cells proliferate with a rate that decreases when the concentration of a critical chemical in the cell environment decreases. At the same time, the progressive depletion of the same chemical increases the tumor cell death rate. A background level of spontaneous cell death is also introduced. Although the model does not include quiescent tumor cells, the onset of quiescence is implicitly represented by the decrease of the proliferation rate. We identify the critical chemical with oxygen, even though glucose and other substances have a fundamental role in the energy metabolism of cells (Bertuzzi et al., 2010). Denoting by $n(x,t)$ the tumor cell density, we can write the following equation:

$$\partial_t n = \underbrace{\nabla\cdot(D_n B(\phi)\nabla n)}_{\text{diffusion}} + \underbrace{B(\phi)\chi(\sigma)n}_{\text{proliferation}} - \underbrace{\mu_n(\sigma)n}_{\text{death}}, \tag{2}$$

where $\sigma(x,t)$ indicates the oxygen concentration. The functions $\chi(\sigma)$ and $\mu_n(\sigma)$ are the per cell rates of proliferation and death respectively, for which we take

$$\chi(\sigma) = A_\chi \frac{\sigma}{K_\chi+\sigma}, \tag{3}$$

and

$$\mu_n(\sigma) = \begin{cases} \bar{\mu}_n cos^2\left(\frac{\pi}{2}\frac{\sigma}{\bar{\sigma}_n}\right)+\mu_0, & \sigma\in[0,\bar{\sigma}_n], \\ \mu_0, & \sigma\in(\bar{\sigma}_n,+\infty), \end{cases} \tag{4}$$

with obvious meaning of the symbols.

As a consequence of the tumor cell metabolism, acidification is observed to occur in the surrounding microenvironment to the extent that it becomes toxic for normal cells favoring the host tissue invasion (Gatenby and Gawlinski, 1996; Gatenby et al., 2003; Fasano et al., 2009). We do not include the dynamics of H^+ ions in the model and we simply represent tumor aggression by assuming that host cells are killed with per cell rate proportional to the local concentration of tumor cells. The normal tissue hosting the tumor is modeled by means of a density $h(x,t)$ of identical cells, which are properly supplied with nutrients by an isotropic network of vessels. For simplicity, the possible renewal process, which implies some proliferative activity to compensate the effect of spontaneous cell death, is disregarded. So, host cells are assumed to be quiescent, devoid of motility, and subjected to cell death only for oxygen deprivation and/or tumor aggression. According to the above assumptions, the equation for $h(x,t)$ reads

$$\partial_t h = \underbrace{-\delta_h n h}_{\text{tumor aggression}} - \underbrace{\mu_h(\sigma) h}_{\text{death by hypoxia}}, \tag{5}$$

where

$$\mu_h(\sigma) = \begin{cases} \bar{\mu}_h cos^2\left(\frac{\pi}{2}\frac{\sigma}{\bar{\sigma}_h}\right), & \sigma \in [0, \bar{\sigma}_h], \\ 0, & \sigma \in (\bar{\sigma}_h, +\infty). \end{cases} \tag{6}$$

It is reasonable that $\bar{\sigma}_h > \bar{\sigma}_n$, in view of the enhanced role of anaerobic metabolism in tumor cells. The value $\bar{\sigma}_h$ has to be taken smaller than the oxygen concentration in the host tissue in the absence of tumor.

2.3. Vasculature and angiogenesis: some key phenomena and assumptions

The present model considers only the microvasculature, which as far as the host tissue is concerned, includes arterioles, capillaries, and venules. In most cases, during tumor invasion, capillaries and venules of the host tissue are eventually destroyed (Vaupel et al., 1989), possibly after transient co-option (Maisonpierre et al., 1997). Arterioles appear to be totally or partially conserved (Vaupel et al., 1989), or more slowly degraded and possibly reformed (Nagy et al., 2009). Host capillaries and venules are replaced by tumor vessels formed upon the angiogenesis process that is stimulated and controlled by a complex interplay among pro-angiogenic and anti-angiogenic factors released by tumor cells and stromal cells (Carmeliet et al., 2011). In some cases, however, the whole host vascular network is co-opted by the tumor and angiogenesis may not occur (Donnem et al., 2013).

The angiogenesis process starts with the formation of sprouts from existing vessels. The tip cell of a sprout appears to be phenotypically distinct from the other endothelial cells (EC) of the sprout, which are termed stalk cells (Geudens and Gerhardt, 2011). The tip cells sense the environment by extending filopodia so as to guide the sprout growth in a direction dictated by chemical gradients. The stalk cells adjacent to the tip proliferate pushing the tip cell forward and generating the endothelial cells that build the sprout body (Ausprunk et al., 1977; Gerhardt et al., 2003; Geudens and Gerhardt, 2011). The remaining stalk cells are quiescent and immobile. As the sprout grows, the stalk cells arrange themselves to form a lumen. Sprouts can form anastomoses with other sprouts, and with newly formed or preformed vessels. After sprout anastomosis, a new vessel is formed allowing blood flow. The newborn vasculature undergoes a maturation process in which some branches regress and others are stabilized. In tumors, however, this vascular remodeling appears abnormal. The newly created vessels, which are the tumor exchange vessels, are generally enlarged and tortuous. Vascular loops can be present and sprouts that do not anastomize can generate tapered and/or leaking vessels. As a consequence, the overall efficiency of the neo-formed tumor vasculature is expected to be poor.

To describe this complex scenario, we make the following assumptions:

- the host arteriolar tree is conserved and incorporated in the tumor;
- host exchange vessels – capillaries and venules – are degraded with a rate proportional to the local density of tumor cells;
- only a single, representative pro-angiogenic factor secreted by the tumor cells is considered (in the following: tumor angiogenic factor, TAF). Anti-angiogenic factors are not included in the model, but they are indirectly taken into account by suitably tuning the TAF degradation rate.
- the pro-angiogenic factor induces the sprouting process by activating the proliferation of the endothelial cells of pre-existing vessels and promotes the cell proliferation in the sprout;
- tumor exchange vessels originate soon after sprout anastomosis. Any vessel maturation stage is disregarded.

Although experimental evidence (Geudens and Gerhardt, 2011) indicates that a number of stalk cells near the tip are actually proliferating in a sprout whereas the tip cells do not divide, for simplicity we assign the mitotic capability to the sprout tip cells and we assume:

- only the tip cell proliferates, with an apparent mitotic rate that accounts for the total proliferative activity occurring in the sprout;
- the tip cells change randomly their orientation with a bias in the direction of the gradient of the TAF concentration.

In the above scheme, after a tip cell mitosis, one daughter cell becomes a quiescent stalk cell, while the other, which has moved forward, becomes the new tip cell. Therefore, in the present model, *only the sprout tip cells are mobile* and we can actually identify the sprout extension with the trajectory traced by the tip cell, as in the "snail-trail" model proposed by Balding and McElwain (1985). Note that, as a consequence of the growth mechanism described above, the tip cell velocity is proportional to the number of proliferating stalk cells and to their mitotic rate. Thus, the tip cells migration mechanism is only partly conditioned by the TAF concentration gradient (in a way that will be discussed at length later on). Since such cells do not move freely, but adhere to the forming vessel, *their speed has a natural upper bound related to the minimal duration of the EC cell cycle and to their size.*Such a picture is also supported by the findings of many experimental and theoretical works where the dependence of the tip cell velocity on the density of proangiogenic factors has been stressed. Among these works, we cite the papers by the Carmeliet research group (see De Smet et al., 2009; Carlier et al., 2012) and the experimental paper by Phng and Gerhardt (2009).

Let us now denote by $w(x,t), z(x,t), v(x,t)$, and $v_h(x,t)$ the densities of sprout tip cells, sprout stalk cells, endothelial cells of tumor vessels, and endothelial cells of host vessels, respectively. The constant density of the arteriolar ECs is indicated by v_a. The average concentration *in the interstitial fluids* of the free pro-angiogenic factor is denoted by $P(x,t)$.

Cells sense the presence of macromolecular chemicals in the surrounding liquid through the occupancy of specific receptors on their surface. Moreover, eukaryotic cells appear to move toward higher chemoattractant concentrations by sensing the difference in the amount of bound receptors across the cell length (Zigmond, 1977; Rivero et al., 1989; Levine et al., 2013). This mechanism exhibits a remarkable sensitivity, as evidenced by experimental

results in which cells were able to respond to chemoattractant concentration differences along the cell as small as 1% (Tranquillo et al., 1988).

In this scenario chemotaxis is driven, in a way that will be discussed, by the TAF concentration gradient, when detectable at the cellular scale. At the macroscopic scale, supposing the receptor-TAF reaction very fast, and supposing the dissociation equilibrium constant K_d of binding equal for all the EC types, we may define the locally averaged fraction $\psi(x,t)$ of the endothelial cell receptors bound to TAF as follows

$$\psi(x,t) = \frac{P(x,t)}{K_d + P(x,t)}. \tag{7}$$

Moreover, we make the reasonable assumption that the "front-tail" difference in the number of bound receptors sensed by the ECs at position x are, in average, proportional to the gradient of $\psi(x,t)$. In conclusion, we assume.

- the EC proliferative activity depends on ψ; the chemotactic signal received by the sprout tip cells depends on the gradient of ψ.

We observe that $\nabla\psi$ and ∇P have the same direction, since

$$\nabla\psi = \frac{K_d}{(K_d+P)^2}\nabla P, \tag{8}$$

and, for an equal $|\nabla P|$, the force of the chemotactic signal decreases as the TAF concentration increases. In fact, when almost all the surface receptors are occupied, their actual distribution is hardly detected by the cells. Experimental evidence of the reduction of chemotactic sensitivity at high TAF concentration is reported by Zigmond (1977) and discussed in Tranquillo et al. (1988). When P is negligible with respect to K_d, $\nabla\psi$ can be considered equal to $\nabla P/K_d$.

To describe the sprouting process, we define a per cell generation rate $\alpha(\psi,\phi)$ representing the per cell rate at which vessel ECs and sprout stalk ECs duplicate during the branching process under the TAF control. Such cell divisions are thought to be asymmetric producing one endothelial cell and one sprout tip cell. For the function $\alpha(\psi,\phi)$ we take the form:

$$\alpha(\psi,\phi) = A_\alpha\psi(1-\psi)^v B(\phi), \tag{9}$$

where A_α denotes the maximal cell proliferation rate and $v \geqslant 0$. When $v > 0$, an inhibition of the EC activation at high concentration of TAF is present, as suggested by *in vitro* experimental observations (Zigmond, 1977). Denoting by u_{tip} the *modulus* of the tip cell velocity, according to our assumptions we have

$$u_{tip}(\psi,\phi) = \Lambda\beta(\psi,\phi), \tag{10}$$

where Λ is the average displacement of a tip cell at each cell duplication, equal to a fraction of the average longitudinal size of proliferating stalk cells contributing to the sprout elongation. The per cell mitotic rate of a tip cell, β, is equal to the mitotic rate of proliferating stalk cells multiplied by their mean number in a sprout. Similarly to Eq. (9), we assume

$$\beta(\psi,\phi) = A_\beta\psi(1-\psi)^v B(\phi). \tag{11}$$

Then, we have $u_{tip} < \Lambda A_\beta$.

2.4. A velocity-jump random walk model for the chemotactic equation of tip cells

Usually, in continuum models of angiogenesis (see Scianna et al., 2013 and references therein), the directed motility of sprout tip cells is described by a chemotactic term linearly dependent on the TAF concentration gradient, according to the Patlak-Keller-Segel model (Patlak, 1953; Keller et al., 1971). However, in view of such linearity, the chemotactic velocity is potentially unbounded, which is physically unacceptable. This limitation of the PKS model has been recognized by Rivero et al. (1989) who derived, in a different biological context and in 1D geometry, alternative models with bounded chemotactic velocity (see also Hillen and Painter, 2009). In the context of angiogenesis, the same kind of approach has been followed by Sun et al. (2005) and Travasso et al. (2011). We remark that u_{tip} depends on ψ and not on $\nabla\psi$. The latter quantity intervenes in selecting the direction of the chemotactic motion.

Now, we derive the chemotactic equation of tip cells by means of a velocity-jump random walk model. Let us start by considering a population of non-interacting cells that move following a "velocity-jump random walk" (Stroock, 1974; Othmer et al., 1988). Unlike the framework commonly used to describe this kind of stochastic process, in which the cell velocity is assumed to change at discrete times taking values in a fixed set of vectors, here we assume that only the velocity direction $\boldsymbol{e} \in \mathscr{S}^{d-1}$ can vary randomly, whereas the velocity modulus is a deterministic function $s(\boldsymbol{x},t)$ of position and time, with $\boldsymbol{x} \in \Omega \subset I\!R^d, d = 2,3$. To describe the cell population, we introduce the cell number density with respect to $\boldsymbol{x}$ and $\boldsymbol{e}$ at time t, which is denoted by $\rho(\boldsymbol{x},\boldsymbol{e},t)$.

Without substantial loss of generality, let us suppose that no cell sources or sinks are present. Then, we can write the following kinetic transport equation for ρ

$$\frac{\partial\rho}{\partial t} + \boldsymbol{e}\cdot\nabla_{\boldsymbol{x}}(s\rho) = -\gamma\rho + \gamma\int_{\mathscr{S}^{d-1}} T(\boldsymbol{e},\boldsymbol{e}')\rho(\boldsymbol{x},\boldsymbol{e}',t)d\boldsymbol{e}', \tag{12}$$

where the turning rate $\gamma(\boldsymbol{x},t)$ is such that $\gamma(\boldsymbol{x},t)dt + o(dt)$ provides the probability that a cell changes its direction between t and $t+dt$, and the turning kernel $T(\boldsymbol{e},\boldsymbol{e}')$ defines the probability of a jump transition from the velocity direction $\boldsymbol{e}'$ to the new velocity direction $\boldsymbol{e}$. Obviously $\int_{\mathscr{S}^{d-1}} T(\boldsymbol{e},\boldsymbol{e}')d\boldsymbol{e} = 1$ to ensure particle conservation.

Next, we derive the transport equations for the first two moments of ρ, defined as

$$\begin{aligned} m_0(\boldsymbol{x},t) &= \int_{\mathscr{S}^{d-1}} \rho(\boldsymbol{x},\boldsymbol{e},t)d\boldsymbol{e}, \\ \boldsymbol{m_1}(\boldsymbol{x},t) &= \int_{\mathscr{S}^{d-1}} \boldsymbol{e}\,\rho(\boldsymbol{x},\boldsymbol{e},t)d\boldsymbol{e}. \end{aligned} \tag{13}$$

By integrating Eq. (12) over $\mathscr{S}^{d-1}$ with respect to $\boldsymbol{e}$, we get

$$\frac{\partial m_0}{\partial t} + \nabla\cdot(s\boldsymbol{m_1}) = -\gamma m_0 + \gamma\int_{\mathscr{S}^{d-1}}\int_{\mathscr{S}^{d-1}} T(\boldsymbol{e},\boldsymbol{e}')\rho(\boldsymbol{x},\boldsymbol{e}',t)d\boldsymbol{e}'d\boldsymbol{e}, \tag{14}$$

where ∇ stands for $\nabla_{\boldsymbol{x}}$. By exchanging the integration order, we recognize that the latter term in Eq. (14) equals γm_0, so that we obtain the following equation for m_0

$$\frac{\partial m_0}{\partial t} + \nabla\cdot(s\boldsymbol{m_1}) = 0. \tag{15}$$

By integrating Eq. (12) multiplied by $s\boldsymbol{e}$ with respect to $\boldsymbol{e} \in \mathscr{S}^{d-1}$, we obtain the equation

$$\begin{aligned} &\int_{\mathscr{S}^{d-1}} s\boldsymbol{e}\frac{\partial\rho}{\partial t}d\boldsymbol{e} + \int_{\mathscr{S}^{d-1}} s\boldsymbol{e}\nabla\cdot(s\boldsymbol{e}\rho)d\boldsymbol{e} \\ &\quad = -\gamma\int_{\mathscr{S}^{d-1}} s\boldsymbol{e}\rho d\boldsymbol{e} + \gamma\int_{\mathscr{S}^{d-1}} s\boldsymbol{e}\int_{\mathscr{S}^{d-1}} T(\boldsymbol{e},\boldsymbol{e}')\rho(\boldsymbol{x},\boldsymbol{e}',t)d\boldsymbol{e}'d\boldsymbol{e}. \end{aligned} \tag{16}$$

For the first term of Eq. (16), we use the equality

$$\begin{aligned} \int_{\mathscr{S}^{d-1}} s\boldsymbol{e}\frac{\partial\rho}{\partial t}d\boldsymbol{e} &= \frac{\partial}{\partial t}\left(\int_{\mathscr{S}^{d-1}} s\boldsymbol{e}\rho d\boldsymbol{e}\right) - \frac{\partial s}{\partial t}\int_{\mathscr{S}^{d-1}} \boldsymbol{e}\rho d\boldsymbol{e} \\ &= \frac{\partial}{\partial t}(s\boldsymbol{m_1}) - \frac{\partial s}{\partial t}\boldsymbol{m_1}, \end{aligned}$$

while the second term of Eq. (16) can be expressed in terms of the dyadic product $\boldsymbol{e}\otimes\boldsymbol{e}$ as follows

$$\begin{aligned}\int_{\mathscr{S}^{d-1}} s\boldsymbol{e}\nabla\cdot(s\boldsymbol{e}\rho)d\boldsymbol{e} &= \int_{\mathscr{S}^{d-1}} s\boldsymbol{e}(\boldsymbol{e}\cdot(s\nabla\rho+\rho\nabla s))d\boldsymbol{e}\\ &= s^2\int_{\mathscr{S}^{d-1}}\boldsymbol{e}(\boldsymbol{e}\cdot\nabla\rho)d\boldsymbol{e}+s\int_{\mathscr{S}^{d-1}}\rho\boldsymbol{e}(\boldsymbol{e}\cdot\nabla s)d\boldsymbol{e}\\ &= s^2\int_{\mathscr{S}^{d-1}}\nabla\cdot(\boldsymbol{e}\otimes\boldsymbol{e}\rho)d\boldsymbol{e}+s\int_{\mathscr{S}^{d-1}}\rho\nabla\cdot(\boldsymbol{e}\otimes\boldsymbol{e}s)d\boldsymbol{e}\\ &= s^2\nabla\cdot\int_{\mathscr{S}^{d-1}}\boldsymbol{e}\otimes\boldsymbol{e}\rho\,d\boldsymbol{e}+s\nabla s\cdot\int_{\mathscr{S}^{d-1}}\boldsymbol{e}\otimes\boldsymbol{e}\rho\,d\boldsymbol{e}.\end{aligned} \tag{17}$$

Since Eq. (17) involves the second order moment of ρ, the system for m_0 and $\boldsymbol{m_1}$ is not closed. Therefore, according to the L^2-moment closure of transport equations (Hillen, 2004; Hillen, 2005; Bellomo et al., 2013), we use the approximation

$$\int_{\mathscr{S}^{d-1}}\boldsymbol{e}\otimes\boldsymbol{e}\rho d\boldsymbol{e}\simeq\frac{1}{d}m_0\boldsymbol{I}, \tag{18}$$

where $\boldsymbol{I}$ is the identity tensor in IR^d, and we get the equality

$$\int_{\mathscr{S}^{d-1}}s\boldsymbol{e}\nabla\cdot(s\boldsymbol{e}\rho)d\boldsymbol{e}=\frac{s^2}{d}\nabla m_0+\frac{s}{d}m_0\nabla s.$$

Moreover, we assume

$$T(\boldsymbol{e},\boldsymbol{e}')=\tilde{T}(\boldsymbol{e}), \tag{19}$$

i.e. the probability of turning to the velocity direction $\boldsymbol{e}$ does not depend on the previous velocity direction of the cell. So, we get to the following equation for the moment $\boldsymbol{m_1}$:

$$\begin{aligned}&\frac{\partial}{\partial t}(s\boldsymbol{m_1})-\frac{\partial s}{\partial t}\boldsymbol{m_1}+\frac{s^2}{\boldsymbol{d}}\nabla m_0+\frac{s}{d}m_0\nabla s\\ &\quad=-\gamma s\boldsymbol{m_1}+\gamma s m_0\int_{\mathscr{S}^{d-1}}\boldsymbol{e}\tilde{T}(\boldsymbol{e})d\boldsymbol{e}.\end{aligned} \tag{20}$$

The moment $\boldsymbol{m_1}$ allows us to express the cell flux $\boldsymbol{J}$ as

$$\boldsymbol{J}(\boldsymbol{x},t)=s(\boldsymbol{x},t)\boldsymbol{m_1}(\boldsymbol{x},t), \tag{21}$$

and using the definition (21) in Eqs. (15), (20), we obtain

$$\frac{\partial m_0}{\partial t}+\nabla\cdot\boldsymbol{J}=0, \tag{22}$$

$$\frac{\partial\boldsymbol{J}}{\partial t}=-\gamma\boldsymbol{J}+\frac{\partial s}{\partial t}\frac{\boldsymbol{J}}{s}-\frac{s^2}{d}\nabla m_0-\frac{s}{d}m_0\nabla s+\gamma s m_0\int_{\mathscr{S}^{d-1}}\boldsymbol{e}\tilde{T}(\boldsymbol{e})d\boldsymbol{e}, \tag{23}$$

that generalizes to $d=2,3$ the model proposed by Rivero et al. (1989) for $d=1$. The last term in the r.h.s. of (23) represents *chemotaxis* as it results from cell tumbling, whereas the term including ∇s gives to the dynamics of the cell flux the contribution of the so called *chemokinesis*.

If one neglects space and time dependence of s in (23), then the system takes the form

$$\begin{aligned}\tfrac{\partial m_0}{\partial t}+&\quad\nabla\cdot\boldsymbol{J}=0,\\ \tfrac{\partial\boldsymbol{J}}{\partial t}=&\quad-\gamma\boldsymbol{J}-\tfrac{s^2}{d}\nabla m_0+\gamma s m_0\textstyle\int_{\mathscr{S}^{d-1}}\boldsymbol{e}\tilde{T}(\boldsymbol{e})d\boldsymbol{e},\end{aligned} \tag{24}$$

which coincides with the one previously derived by Hillen (2004) and Perthame (2004) starting directly from the assumption of a constant velocity modulus.

Let us now specialize the previous argument in order to derive a tip cell chemotactic equation of the kind described in Section 2. So, let $\rho(\boldsymbol{x},\boldsymbol{e},t)$ denote the sprout tip cell density with respect to $\boldsymbol{x}$ and $\boldsymbol{e}$. Setting $d=3$ and slightly simplifying the notation, we take $m_0(\boldsymbol{x},t)=w(x,t)$ and

$$s(\boldsymbol{x},t)=u_{tip}(\psi(x,t),\phi(x,t)).$$

Moreover, Eqs. (22) and (23) will now include source and sink terms representing the processes of branching and anastomosis. Assuming that source and sink are independent of $\boldsymbol{e}$, we get the system

$$\frac{\partial w}{\partial t}+\nabla\cdot\boldsymbol{J}=\alpha(\psi,\phi)(v_h+v+z)-\kappa_{an}(v_a+v_h+w+z+v)w-\mu_w w, \tag{25}$$

$$\frac{\partial\boldsymbol{J}}{\partial t}=-\gamma\boldsymbol{J}+\frac{1}{u_{tip}}\frac{\partial u_{tip}}{\partial t}\boldsymbol{J}-\frac{u_{tip}^2}{3}\nabla w-\frac{u_{tip}}{3}w\nabla u_{tip}+\gamma u_{tip}w\int_{\mathscr{S}^2}\boldsymbol{e}\tilde{T}(\boldsymbol{e})d\boldsymbol{e}, \tag{26}$$

where the generation term $\alpha(\psi,\phi)$ is given by (9).

Following Rivero et al. (1989), we consider the quasi-stationary state approximation of Eq. (26), neglecting the terms dependent on the u_{tip} derivatives. Setting $\int_{\mathscr{S}^2}\boldsymbol{e}\tilde{T}(\boldsymbol{e})d\boldsymbol{e}=\mathscr{C}(\nabla\psi)$, we get

$$\boldsymbol{J}=-\frac{u_{tip}^2}{3\gamma}\nabla w+u_{tip}\mathscr{C}(\nabla\psi)w. \tag{27}$$

In our approach, still following Rivero et al. (1989), we take $\tilde{T}(\boldsymbol{e})=p(\boldsymbol{e};\nabla\psi)$ and, in agreement with the choice (31), we suppose that p is such that

$$\int_{\mathscr{S}^2}\boldsymbol{e}\,p(\boldsymbol{e};\nabla\psi)d\boldsymbol{e}=\frac{\nabla\psi}{K_q+|\nabla\psi|}. \tag{28}$$

An example of probability density function complying with (28) is

$$\hat{p}(\boldsymbol{e};\nabla\psi)=\left(1-\frac{|\nabla\psi|}{K_q+|\nabla\psi|}\right)U(\boldsymbol{e})+\frac{|\nabla\psi|}{K_q+|\nabla\psi|}\delta\left(\boldsymbol{e}-\frac{\nabla\psi}{|\nabla\psi|}\right),$$

where $U(\cdot)$ is a uniform density in $\mathscr{S}^2$ and $\delta(\cdot)$ is the Dirac distribution. Then, we have

$$J_w=-D_w(\psi,\phi)\nabla w+u_{tip}(\psi,\phi)q(|\nabla\psi|)\frac{\nabla\psi}{|\nabla\psi|}w. \tag{29}$$

The function $D_w(\psi,\phi)$ in (29) is given by

$$D_w(\psi,\phi)=\frac{u_{tip}^2(\psi,\phi)}{3\gamma}, \tag{30}$$

In the expressions above, the crowding effect, which everywhere else is introduced by means of the factor $B(\phi)$, is actually included in u_{tip}, as shown by Eqs.(10), (11). Finally, as suggested by Rivero et al. (1989), we take

$$q(|\nabla\psi|)=\frac{|\nabla\psi|}{K_q+|\nabla\psi|}, \tag{31}$$

where $1/K_q$ is the chemotactic sensitivity.

2.5. The model for the dynamics of vessel cell densities

We can now write the equations for the cell densities w,z, and v, obtaining

$$\begin{aligned}\partial_t w=&\underbrace{\nabla\cdot(D_w(\psi,\phi)\nabla w)}_{\text{diffusion}}-\underbrace{\nabla\cdot\left(u_{tip}(\psi,\phi)q(|\nabla\psi|)\frac{\nabla\psi}{|\nabla\psi|}w\right)}_{\text{chemotaxis}}\\ &+\underbrace{\alpha(\psi,\phi)(v_h+v)}_{\text{generation}}-\underbrace{\kappa_{an}(v_a+v_h+w+z+v)w}_{\text{anastomosis}}-\underbrace{\mu_w w}_{\text{death}},\end{aligned} \tag{32}$$

$$\partial_t z=\underbrace{\beta(\psi,\phi)w}_{\text{proliferation}}-\underbrace{\kappa_{an}(v_a+v_h+w+z+v)z}_{\text{transition z}\to v}-\underbrace{\mu_z z}_{\text{death}}, \tag{33}$$

$$\partial_t v=\underbrace{\kappa_{an}(v_a+v_h+w+z+v)(z+w)}_{\text{transition z+w}\to v}-\underbrace{\mu_v v}_{\text{death}}. \tag{34}$$

Note that since $\kappa_{an}(v_a+v_h+w+z+v)$ is the per cell rate at which tip cells anastomize, such a rate is assumed to be the per cell rate at which sprout cells becomes cells belonging to tumor vessels.

Concerning the dynamics of host vessels, we write:

$$\partial_t v_h=\underbrace{-\delta_{v_h}n\,v_h}_{\text{tumor aggression}} \tag{35}$$

The balance between the degradation of host vessels and the degradation of host tissue cells it is likely to control the extent of host vessel co-option. Indeed, if the rate δ_{v_h} is smaller than the rate

δ_h the tumor can advance in a space that still contain host vessels. If $\delta_{v_h} > 0$, the vessel co-option is anyway transient and the co-opted host vessels are eventually destroyed. If instead $\delta_{v_h} > \delta_h$, host vessel co-option should occur to a minimal extent.

2.6. Dead cells

For simplicity, all the dead cells, irrespectively of their origin, are assumed to degrade in situ into liquids following a first order kinetics with the same rate constant λ_m:

$$\partial_t m = \mu_n(\sigma)n + \mu_h(\sigma)h + \mu_w w + \mu_z z + \mu_v v + \delta_h nh + \delta_{v_h} n v_h - \underbrace{\lambda_m m}_{\text{dissolution}}. \tag{36}$$

2.7. Chemicals

Oxygen The dynamics of oxygen must express the balance among its diffusion, supply, and consumption. Since oxygen appears capable of crossing the cell membrane freely, we assume that oxygen diffuses in the whole space domain with constant diffusivity D_σ. The mean oxygen concentration in the tissue is represented by the variable $\sigma(x,t)$. Oxygen supply to tissues is described by means of two diffuse sources that mimic the oxygen efflux from the host and the tumor vasculature, respectively. Both the source intensities are taken proportional to the local vascular extent (v_h and v, respectively) and to the difference between the (constant) average intravascular oxygen concentration and $\sigma(x,t)$:

$$\gamma_h v_h(x,t)\big(\sigma_h^* - \sigma(x,t)\big), \qquad \gamma_v v(x,t)\big(\sigma_v^* - \sigma(x,t)\big),$$

where σ_h^* and σ_v^* denote the mean oxygen concentration into healthy and tumor vessels, respectively, while γ_h and γ_v denote the related proportionality coefficients. We disregard the contribution to oxygen supply of arterioles, since their exchange surface is much less than the one of the remaining microvasculature.

Although the oxygen concentrations in afferent arterioles of host and neo-formed vasculature may be the same, the model includes different values of σ_h^* and σ_v^* to reflect different blood flow rate in the two vascular network. Given the dysfunctional nature of the neo-formed vessel network, we take $\sigma_h^* > \sigma_v^*$.

The oxygen consumption by tumor and host cells, for simplicity, is supposed to depend on the oxygen concentration according to the same Michaelis–Menten law. The oxygen consumption of the ECs forming vessels and sprouts, instead, is assumed not to affect the dynamics of σ, since these cells take oxygen directly from blood. We then may write the equation

$$\partial_t \sigma = \underbrace{D_\sigma \nabla^2 \sigma}_{\text{diffusion}} + \underbrace{\gamma_h v_h\big(\sigma_h^* - \sigma\big) + \gamma_v v\big(\sigma_v^* - \sigma\big)}_{\text{supply from } v_h,\, v} - \underbrace{\big(H_n(\sigma)n + H_h(\sigma)h\big)}_{\text{consumption by tumor and healthy cells}}, \tag{37}$$

where the per cell oxygen consumption rate is modeled as

$$H_i(\sigma) = A_{Hi}\frac{\sigma}{K_{Hi} + \sigma}, \qquad i = n, h. \tag{38}$$

Pro-angiogenic factor Pro-angiogenic factors are macromolecules that find a barrier in the cell membrane and in the ECM. Thus, their diffusion occurs through the interstitial liquid only (Krol et al., 1999). We express the TAF available volume fraction as $\phi_P^* - \phi(x,t)$, where $\phi_P^* \leqslant 1 - \phi_{ECM}$ is the interstitial liquid volume fraction in the absence of cells and vessels. It is reasonable that the space available for cells and vessels is reduced by the ECM to a greater extent than the space available for TAF. So, we take $\phi_P^* > \phi^*$, which guarantees a positive lower bound to the TAF available volume fraction even when $\phi = \phi^*$.

Important pro-angiogenic factors, such as VEGF, are produced also by non-tumoral cells, so that they can be present in the body even in the absence of tumors. Nevertheless, in the present model we assume that *only* tumor cells produce TAF and that the secretion rate increases as the oxygen concentration (inside and around the cell) decreases.

The derivation of the equation for the average TAF concentration $P(x,t)$ in the available space requires some attention since the volume fraction available for TAF can change in space and time. Let us consider a generic compact subdomain $\mathscr{A} \subset \Omega$. We assume that the fraction of elementary surface around x on $\partial\mathscr{A}$ available for the flow of TAF molecules is equal to the available volume fraction at x, for any surface orientation. Moreover, we assume that the average gradient of the microscopic interstitial TAF concentration on the elementary surface portion that allows the flow, is well approximated by the gradient of $P(x,t)$. Therefore the outflow from the boundary of $\mathscr{A}$ is expressed as

$$-D_P \int_{\partial\mathscr{A}} e(x)\cdot\nabla P(x,t)\big(\phi_P^* - \phi(x,t)\big)dS,$$

where D_P is the TAF diffusivity in the interstitial fluids and $e(x)$ denotes the outward normal. In addition, the amount of TAF contained in $\mathscr{A}$ is given by

$$\int_{\mathscr{A}} P(x,t)\big(\phi_P^* - \phi(x,t)\big)dx.$$

Taking into account that $\mathscr{A}$ is a generic set, the following balance equation can be derived by means of standard arguments:

$$\partial_t\big((\phi_P^* - \phi)P\big) = \underbrace{\nabla\cdot\big(D_P(\phi_P^* - \phi)\nabla P\big)}_{\text{diffusion through interstices}} + \underbrace{\pi_P(\sigma)n}_{\text{production}} - \underbrace{C_P(P)(v_h + v + z + w)}_{\text{consumption by ECs}} - \underbrace{\lambda_P P\big(\phi_P^* - \phi\big)}_{\text{degradation}}, \tag{39}$$

Since after internalization into EC cytoplasm the angiogenic factor is rapidly degraded, no TAF outflow from ECs is allowed. The per cell production rate $\pi_P(\sigma)$ is described by

$$\pi_P(\sigma) = A_\pi\frac{K_\pi}{K_\pi + \sigma}, \tag{40}$$

whereas, taking into account that only the receptor-bound TAF is internalized and degraded by the endothelial cells (Mac Gabhann and Popel, 2004) we assume C_P proportional to ψ, so that recalling (7), we write

$$C_P(P) = A_C\frac{P}{K_d + P}. \tag{41}$$

An explicit account of the possible washout of TAF through the vasculature is omitted because of the lack of specific experimental information. We rather incorporate this phenomenon in the choice of the parameter λ_P. We may note, however, that in case of VEGF the fast spontaneous loss of bioactivity (Serini et al., 2003) could overcome the loss through the vascular washout.

2.8. The volume fraction ϕ

In order to close the system, it remains to specify $\phi(x,t)$. We assume for simplicity that all cells have the same volume V_c and that the ratios of the volume fractions of arterioles, host exchange vessels, tumor exchange vessels, and sprouts to the volume fractions of the cells forming them have the same average value K. Then, the local fraction of volume ϕ is given by

$$\phi = V_c(n + h + m + K(v_a + v_h + v + w + z)). \tag{42}$$

In the formula above we are treating arterioles as they were similar to the other vessels, which is not the case. Thus, the quantity v_a represents an equivalent concentration providing the actual experimental value for the corresponding volume fraction.

Remark 1. It is to be noted that for the physical consistency of the model it is necessary that $\phi(x,t)$ does not exceed ϕ^*. The proof of this property, along with the proof of the non-negativity of all the quantities representing cellular densities, is given in Appendix A under the hypothesis that the equation system, with the boundary and initial conditions specified below, has one unique classical solution in the class $\mathscr{C}^{2,1}(\Omega\times(0,T))$. The proof of the wellposedness of the model is instead beyond the scope of this paper.

2.9. Boundary and initial conditions

Eqs. (2), (32), (37), (39) are completed by the following conditions on $\partial\Omega$ for $t>0$:

$$\begin{aligned} &n(x,t)=0,\\ &w(x,t)=0,\\ &\sigma(x,t)=\sigma_{ff},\\ &P(x,t)=0. \end{aligned} \tag{43}$$

The null boundary conditions for n, w, and P are justified if the domain Ω is taken sufficiently large to guarantee, along with suitable initial conditions such as those described below, that the tumor remains substantially "far" from the boundary in the considered time interval $[0,T]$. Concerning the oxygen, $\sigma_{ff}>0$ is a far field concentration that we identify with the stationary oxygen concentration in the host tissue in the absence of tumor.

The initial conditions are given by continuous, bounded, and non-negative functions $n^0(x), h^0(x), m^0, v_h^0(x), w^0(x), z^0(x), v^0(x)$, and $\sigma^0(x), P^0(x)$. The cell densities must be such that ϕ, defined by (42), satisfies the property $0<\phi(x,0)<\phi^*$ for any x in Ω. Moreover, on $\partial\Omega$, the compatibility conditions

$$\begin{aligned} &n^0(x)=0,\\ &w^0(x)=0,\\ &\sigma^0(x)=\sigma_{ff},\\ &P^0(x)=0, \end{aligned} \tag{44}$$

are required.

In addition, since the boundary of Ω is supposed to be "far" from the tumor, we choose to have $n^0(x), w^0(x), z^0(x), v^0(x)$ identically equal to zero in a rather large portion of Ω, which is adjacent and includes $\partial\Omega$.

3. Numerical simulation

The model is studied numerically in spherical symmetry. Moreover, we take a quasi-steady state assumption for the dynamics of oxygen, since the diffusion coefficient of this chemical is much larger than the diffusivities of either cells and TAF. On the contrary, typical values of the TAF diffusion coefficient are not such to guarantee the validity of the quasi-steady state assumption for the TAF dynamics.

Let the spatial domain be a sphere of radius R. In spherical symmetry, all the cell densities and the chemical concentration are functions of the radial distance r and t, and the model equations, for $r\in(0,R)$ and $t\in(0,T)$, become:

$$\begin{aligned} &\frac{\partial n}{\partial t}=\frac{1}{r^2}\frac{\partial}{\partial r}\left(r^2 D_n B(\phi)\frac{\partial n}{\partial r}\right)+B(\phi)\chi(\sigma)n-\mu_n(\sigma)n,\\ &\frac{\partial h}{\partial t}=-\delta_h n h-\mu_h(\sigma)h,\\ &\frac{\partial w}{\partial t}=\frac{1}{r^2}\frac{\partial}{\partial r}(r^2 D_w(\psi,\phi)\nabla w)-\frac{1}{r^2}\frac{\partial}{\partial r}\left(r^2 u_{tip}(\psi,\phi)q\left(|\frac{\partial\psi}{\partial r}|\right)\mathrm{sign}\left(\frac{\partial\psi}{\partial r}\right)\mathrm{w}\right)\\ &+\alpha(\psi,\phi)(v_h+v)\\ &-\kappa_{an}(v_a+v_h+w+z+v)w-\mu_w w,\\ &\frac{\partial z}{\partial t}=\beta(\psi,\phi)w-\kappa_{an}(v_a+v_h+w+z+v)z-\mu_z z,\\ &\frac{\partial v}{\partial t}=\kappa_{an}(v_a+v_h+w+z+v)(z+w)-\mu_v v,\\ &\frac{\partial m}{\partial t}=\mu_n(\sigma)n+\mu_h(\sigma)h+\mu_w w+\mu_z z+\mu_v v+\delta_h n h+\delta_{v_h} n v_h-\lambda_m m,\\ &0=D_\sigma\frac{1}{r^2}\frac{\partial}{\partial r}\left(r^2\frac{\partial\sigma}{\partial r}\right)+\gamma_h v_h(\sigma_h^*-\sigma)+\gamma_v v(\sigma_v^*-\sigma)\\ &-H_n(\sigma)n-H_h(\sigma)h,\\ &\frac{\partial P}{\partial t}=\frac{1}{r^2}\frac{\partial}{\partial r}\left(D_P(\phi_P^*-\phi)\frac{\partial P}{\partial r}\right)+\pi_P(\sigma)n+P\frac{\partial\phi}{\partial t}\\ &-C_P(P)(v_h+v+z+w)-\lambda_P P. \end{aligned} \tag{45}$$

Denoting by $n^0(r), h^0(r), m^0(r), v_h^0(r), w^0(r), z^0(r), v^0(r)$ the initial distributions of cells in $[0,R]$, we assume

$$n^0(r)=\begin{cases}\bar n & r\in[0,R_0]\\ \bar n\cos^2\left(\frac{\pi}{2}\frac{r-R_0}{R_1-R_0}\right) & r\in(R_0,R_1]\\ 0 & r\in(R_1,R],\end{cases} \tag{46}$$

$$h^0(r)=\begin{cases}0 & r\in[0,R_0]\\ \bar h\sin^2\left(\frac{\pi}{2}\frac{r-R_0}{R_1-R_0}\right) & r\in(R_0,R_1]\\ \bar h & r\in(R_1,R],\end{cases} \tag{47}$$

$$v_h^0(r)=\begin{cases}0 & r\in[0,R_0]\\ \bar v_h\sin^2\left(\frac{\pi}{2}\frac{r-R_0}{R_1-R_0}\right) & r\in(R_0,R_1]\\ \bar v_h & r\in(R_1,R],\end{cases} \tag{48}$$

and

$$m^0(r)=w^0(r)=z^0(r)=v^0(r)\equiv 0,\quad r\in[0,R], \tag{49}$$

with $\bar n, \bar h$, and $\bar v_h$ such that $\phi(r,0)<\phi^*$, and $\bar n>n^*, n^*$ denoting a minimal threshold concentration of tumor cells allowing to identify the tumor. We thus have a central subdomain $[0,R_0]$ representing an initial *avascular* tumor nodule, whose radius R_0 can be taken sufficiently small to justify $m^0\equiv 0$. This tumoral core is surrounded by a small transition zone $[R_0,R_1]$ in which n^0 decreases to zero, while h^0 and v_h^0 increase from 0 to the values respectively taken in the outer domain $(R_1,R]$.

Concerning the boundary conditions, all the mobile species are subject to zero flux boundary conditions at $r=0$ because of symmetry

$$\frac{\partial n}{\partial r}|_{r=0}=\frac{\partial w}{\partial r}|_{r=0}=\frac{\partial\sigma}{\partial r}|_{r=0}=\frac{\partial P}{\partial r}|_{r=0}=0,$$

whereas at $r=R$ we impose (43).

For the numerical solution of Eqs. (2) and (32) an explicit finite-difference, forward in time, scheme was implemented. To discretize the chemotactic term in Eq. (32), we adopted the upwind explicit scheme of the paper by Tsyganov et al. (2004). The solution of the equations for oxygen and TAF was obtained by using the Gauss–Seidel iterative method.

Table 1
Baseline parameter values.

General parameters		
ϕ^*	0.85	See text
p	1.1	See text
V_c	$2.145 \cdot 10^{-9}$ cm^3	Freyer and Sutherland (1985)
Λ	$8.0 \cdot 10^{-4}$ cm	Krüger-Genge et al. (2019)
r_0	$1.0 \cdot 10^{-3}$ cm	Welter et al. (2008)
δ	$2 \cdot 10^{-4}$ cm	Krüger-Genge et al. (2019)
K	3.27	See text
$K\phi_{v_a}$	$4.0 \cdot 10^{-3}$	See text
λ_m	$2.08 \cdot 10^{-2}$ h^{-1}	Darzynkiewicz et al. (1997)
Oxygen		
D_σ	$7.2 \cdot 10^{-2}$ cm$^2 \cdot$ h^{-1}	Stamper et al. (2010)
σ_h^*	$7.62 \cdot 10^{-5}$M (=60 mmHg)	Vaupel et al. (1991)
σ_v^*	$4.45 \cdot 10^{-5}$ M (=35 mmHg)	Vaupel et al. (1991)
γ_h, γ_v	$1.86 \cdot 10^{-3}$ h^{-1} cm^3	Casciari et al. (1992)
A_{Hn}, A_{Hh}	$2.99 \cdot 10^{-13}$ mol $\cdot$ h^{-1}	Freyer and Sutherland (1985)
K_{Hn}, K_{Hh}	$4.64 \cdot 10^{-6}$ M	Casciari et al. (1992)
Tumor and host tissue		
D_n	$3.6 \cdot 10^{-7}$ cm$^2 \cdot$ h^{-1}	Stamper et al. (2010)
A_χ	$2.88 \cdot 10^{-2}$ h^{-1}	Bertuzzi et al. (2003)
K_χ	$5.08 \cdot 10^{-6}$ M (=4 mmHg)	Bertuzzi et al. (2003)
$\bar{\sigma}_n$	$2.54 \cdot 10^{-6}$M (=2 mmHg)	Freyer and Sutherland (1986)
$\bar{\mu}_n$	5 (ln 2/24)=0.144 h^{-1}	Franko et al. (1978)
μ_0	ln 2/(10 $\cdot$ 24)=$2.88 \cdot 10^{-3}$ h^{-1}	See text
δ_h, δ_{v_h}	$4 \cdot 10^{-9}$ h$^{-1} \cdot$ cm^3	Gatenby and Gawlinski (1996)
$\bar{\sigma}_h$	$3.81 \cdot 10^{-6}$M (=3 mmHg)	See text
$\bar{\mu}_h$	5 (ln 2/24)=0.144 h^{-1}	See text
Angiogenesis and TAF		
ϕ_P^*	0.90	See text
K_d	$5.75 \cdot 10^{-10}$ M	Swanson et al. (2011)
A_α	$2.88 \cdot 10^{-2}$ h^{-1}	Bertuzzi et al. (2003)
A_β	$1.15 \cdot 10^{-1}$ h^{-1}	Chaplain et al. (1993) and Stamper et al. (2010)
ν	1	See text
D_P	$1.8 \cdot 10^{-3}$ cm$^2 \cdot$ h^{-1}	Anderson et al. (2000)
A_π	$5.96 \cdot 10^{-19}$ mol $\cdot$h^{-1} (per cell)	Swanson et al. (2011)
K_π	$4.45 \cdot 10^{-5}$ M (=35 mmHg)	Assumed
A_C	$3.86 \cdot 10^{-19}$ mol $\cdot$h^{-1} (per cell)	Mac Gabhann and Popel (2004)
λ_P	0.65 h^{-1}	Serini et al. (2003)
Vasculature		
γ	0.1 h^{-1}	See text
K_q	$5 \cdot 10^4$ cm^{-1}	Rivero et al. (1989)
κ_{an}	$4 \cdot 10^{-9}$ cm$^3 \cdot$ cell$^{-1} \cdot$ h^{-1}	Assumed
μ_v	$1.0 \cdot 10^{-3}$ h^{-1}	Chaplain et al. (1993)
μ_w, μ_z	$5 \cdot 10^{-4}$ h^{-1}	See text

4. Parameter values

The baseline values of parameters are reported in Table 1. Here, some comments on their choice follow.

Volume fraction of ECM, cells and vasculature The mean cellular volume V_c is assumed equivalent to the volume of a sphere with diameter 16μm, irrespective of the cell tissue type or shape. With this choice, we get $V_c = 2.145 \cdot 10^{-9}$ cm^3 (see Table 1) in agreement with the experimental data in Freyer and Sutherland (1985). Assuming such a relatively small mean cellular volume is a suitable choice in our model, which is written in terms of local volume fractions. The same value of V_c is also compatible with the size range experimentally measured for the endothelial cells (see for instance the review by Krüger-Genge et al. (2019)). Coming to the parameter K, we recall that it represents the mean ratio between the volume fraction of vessels of any kind and the volume fraction of the cells constituting the vessels. To estimate K, we supposed all the vasculature (including the sprouts developed during angiogenesis) ideally decomposed in identical cylindrical units of inner radius r_0, wall thickness δ, and length L. Thus, $\pi(r_0+\delta)^2 L$ is the volume of the vessel unit, whereas $\pi\left[(r_0+\delta)^2 - r_0^2\right]L$ is the volume of the vessel wall, and then of the ECs lining the lumen. Therefore, from the ratio between these volumes, we get

$$K = \frac{(r_0+\delta)^2}{\delta(2r_0+\delta)},$$

which, assuming $r_0 = 10$ μm and $\delta = 2$ μm, provides the value $K = 3.27$ reported in Table 1.

The volume fractions of ECM, cells and vasculature vary with the tissue type, and the measured values often change also with the measurement technique. In humans, the ECM volume fraction have been found to range from 3% in healthy liver to 15–20% in brain (Ariza de Schellenberger et al., 2018). Values of the cell volume fraction of 76% in rat liver (Donahue et al., 1995) and 56% in rat brain (Buckley et al., 1999) were measured by MRI, whereas a value of 69% was found in rat tumors (Donahue et al., 1995). In human brain tumors, PET measurements of extracellular space reported by Bruehlmeier et al. (2003) suggest a cell volume fraction in the range 39%–56%. According to these data, we assume $\phi_{ECM} = 0.1, \phi^* = 0.85$, and for the initial non-zero values of ϕ_h and ϕ_n the values 0.65 and 0.6, respectively.

Concerning the blood volume fraction, values ranging from 2.7% to 7.0% are reported for human tissues (see e.g. Ito et al., 2001; Lai et al., 2009), while in vivo MRI measurements in rat healthy and tumor brain tissues yielded fraction values in the range of 2% to 4% (Perles-Barbacaru et al., 2012). Some of these studies provide measures of the arterial percentage of the total blood volume fraction, noting in addition that the arterial fraction remains relatively constant in time (Lai et al., 2009). An arterial percentage of about 10% in skeletal muscle blood volume is measured by Lai et al. (2009) using near-infrared spectroscopy, whereas a 20% arterial percentage is found in other organs (for instance human liver (Hashimoto et al., 2006)). Overall, these experimental findings suggest values of $4-5\%$ for the total (capillaries, venules, and arterioles) blood volume fraction in the host tissue. Hence, we set an initial non-zero value of ϕ_{v_h} equal to 0.04. Moreover, we will assume a constant arteriolar fraction equal to 10% of the total. Assuming the lower measured value is justified by the reduction of the arterial part of the vasculature which likely occurs eventually during the tumor evolution, but which is not represented in our dynamical model.

Tip cell motion Concerning the choice of γ, we start from the remark (Rivero et al., 1989) that the time $1/\gamma$ (persistence time) has to be substantially smaller than the "observation time" of the tumor progression, since this guarantees that the approximations leading to (27) are feasible. If the observation time is chosen to be 10 days (a time over which changes in the system can be observed), an acceptable choice is $\gamma = 0.1\text{h}^{-1}$. The 10 h persistence time appears a reasonable choice if compared with the 24 h time scale for cells replication. A larger time (e.g. 50 h) would basically suppress the chemotactic random component, a shorter time (e.g. 1 h) would mitigate the constraint around the main orientation in an excessive way.

Cell death rates According to Eqs. (4), (6), the oxygen-dependent death rates $\mu_n(\sigma), \mu_h(\sigma)$ are assumed to be decreasing

functions of σ. We further assume that cells die (with maximal rates $\bar{\mu}_n, \bar{\mu}_h$) when the oxygen concentration falls below critical values (here denoted by $\bar{\sigma}_n, \bar{\sigma}_h$, respectively) that we deduced from experimental literature data (Franko et al., 1978; Freyer and Sutherland, 1986, see Table 1). The remaining parameters of $\mu_n(\sigma), \mu_h(\sigma)$ were inferred either from the mentioned experimental data or from estimates obtained in our previous works on tumor growth (Bertuzzi et al., 2010). So, we fixed $\bar{\mu}_h = \bar{\mu}_n$ and μ_0 equal to a fraction of $\bar{\mu}_n$, also choosing $\bar{\sigma}_h$ as indicated in Section 2. Finally, in the absence of direct information on the death rates of sprout cells, we fixed $\mu_w = \mu_z = 0.5\mu_v$ (μ_v as in Chaplain et al. (1993)).

5. Computational results

The numerical solution of our model has been computed according to the scheme depicted in Section 3 within a spherical spatial domain of radius $R = 1$ cm and over a time interval $T = 360$ days. Eqs. (45) have been solved using the boundary and initial conditions (43), (44), and assuming the baseline parameter values of Table 1. For the remaining parameters of the initial distributions we set: initial tumor radius $R_0 = 0.02$ cm, external radius of the tumor-host interstitial gap $R_1 = 0.03$ cm, local volume fractions $V_c\bar{n} = V_c\bar{h} = 0.6, KV_c\bar{v}_h = 0.04$, and $K\phi_{v_a} = 0.1 \times KV_c\bar{v}_h = 4 \cdot 10^{-3}$. The initial oxygen distribution is computed as the quasi-stationary solution of the oxygen diffusion equation in system (45), imposing zero flux condition $\partial\sigma/\partial r = 0$ at $r = 0$ and prescribing a constant "far field" value $\sigma_{ff} > 0$ at $r = R$. The concentration $\sigma_{ff} > 0$ satisfies the equation

$$\gamma_h\bar{v}_h(\sigma_h^* - \sigma_{ff}) - H_h(\sigma_{ff})\bar{h} = 0,$$

with $H_h(\sigma)$ given by Eq. (38). In the present simulation, $\sigma_{ff} = 7.03 \cdot 10^{-5}$ M (51.37 mmHg).

The time course of the chemical quantities σ and P are plotted in Fig. 1 from the initial time $t = 0$ up to 360 days, with time step 120 days.

With the same criterion, Figs. 2 and 3 illustrate the evolution of the spatial distributions of cell populations towards the steady state and the host invasion by the tumor. More precisely, denoting by p the generic cell population density, in the following figures we plot the corresponding local volume fraction ϕ_p, defined as

$$\phi_p = V_c\, p, \qquad p = n, h, m, v_a, v_h, w, z, v. \tag{50}$$

Using this notation for all cell and vessel quantities, in Fig. 2 we plot the behaviors of the local volume fractions of host cells ϕ_h, tumor cells ϕ_n, dead cells ϕ_m, and of the total volume fraction ϕ (see (42)).

Fig. 3 illustrates the formation of the tumor neovasculature, which proceeds simultaneously to the tumor growth, reporting the local volume fractions of vessels in the tumor and host tissue. In particular, the left panels of Fig. 3 report the local volume fractions of host and tumor vessels, $K\phi_{v_h}$ and $K\phi_v$ respectively, while the right panels report the patterns of $K\phi_w$ and $K\phi_z$.

The simulation shows that the tumor progression takes the form of a traveling wave. The wave front profile propagates with velocity approximately equal to 20μm per day, as it could be expected in view of the chosen values of the proliferation rate and cellular diameter.

As studied analytically in Appendix B, numerical simulations eventually develop into a steady state in which healthy cells and vessels (ϕ_h, ϕ_{v_h}) have been eliminated and supplanted by a neovascularized tumor. The numerical solution after 360 days (see bot-

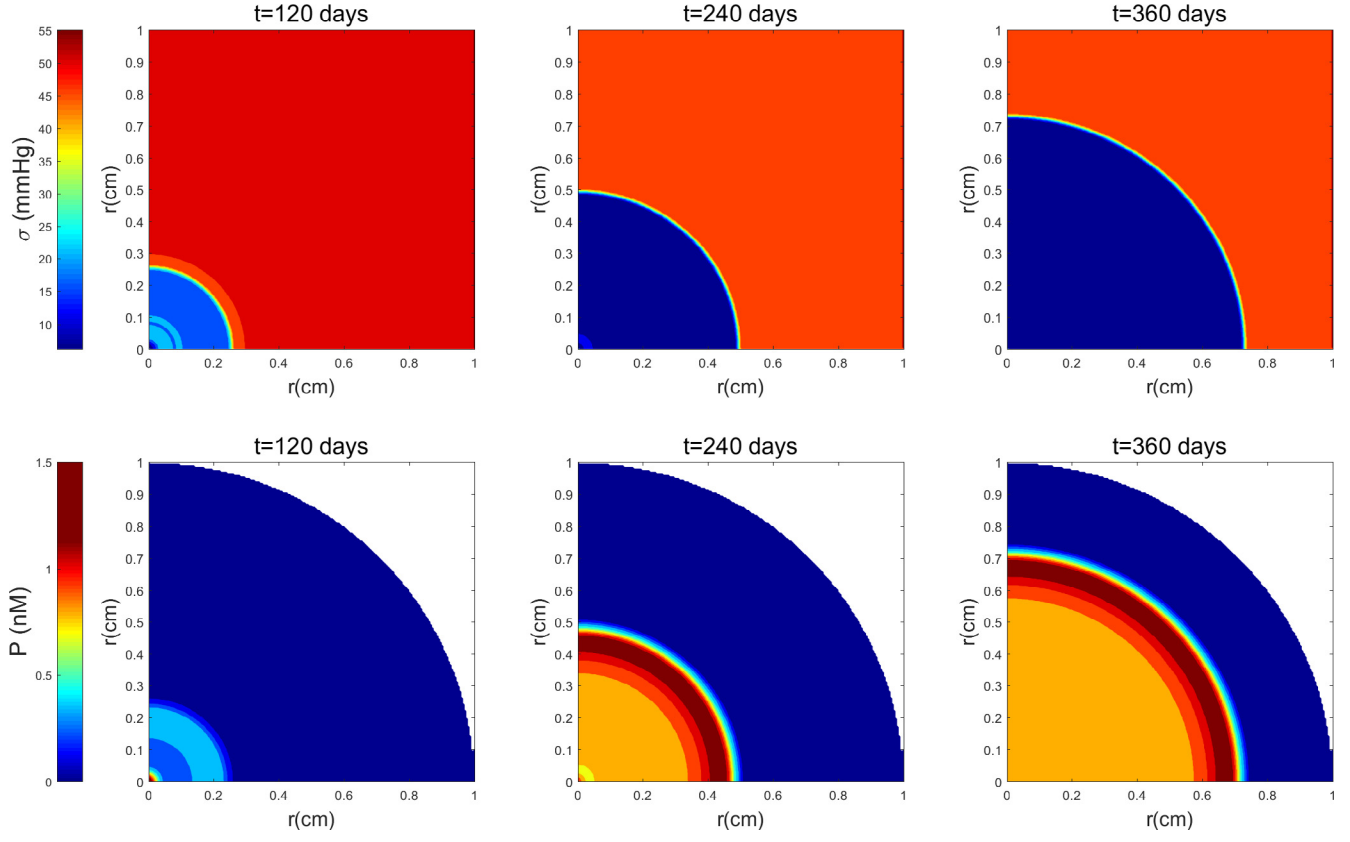

Fig. 1. Evolution of the chemical concentrations in a spherical domain of radius $R = 1$ cm up to 360 days. Upper panels: oxygen concentration (mmHg), lower panels: TAF concentration (nM).

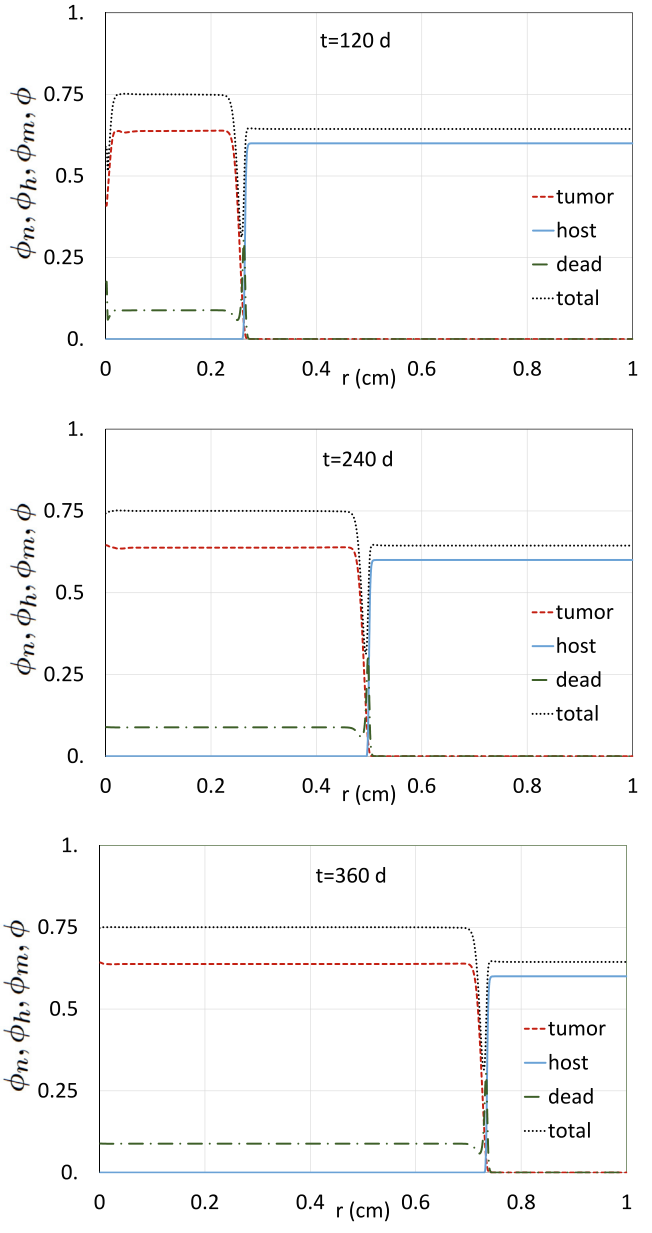

Fig. 2. Simulated evolution of the local volume fractions of cells: ϕ_n (tumor, dashed line); ϕ_h (host, solid line); ϕ_m (dead, dot-dashed line); ϕ (total volume fraction, dotted line).

tom panels of Figs. 2, 3) indicates that all quantities tend to become constant in time and space attaining the following values: $\sigma = 21.1$ mmHg, $P = 0.27$ nM, $\psi = 0.32, \phi_n = 0.64, K\phi_v = 1.9 \cdot 10^{-2}, K\phi_w = 9.1 \cdot 10^{-4}, K\phi_z = 3.6 \cdot 10^{-4}, \phi_m = 8.8 \cdot 10^{-2}, \phi = 0.75$.

From the previous set of values, and using (50), we evaluated the corresponding model variables and we verified that the obtained set is a solution to the system of equations given in Appendix B. One more remark which is in order is the fact that in Fig. 2 the wave front exhibits coexistence of healthy and tumor cells. The model by Gatenby and Gawlinski (1996) was conceived to account for a necrotic gap appearing in some kind of tumor. The possible onset of such a gap is related to the strength of the tumor aggression, i.e. to the value of the parameter δ_h in our model. As proven in Fasano et al. (2009), the gap is replaced by an overlapping zone if δ_h is not large enough. We could have made a gap appear by choosing a larger δ_h.

There are papers reporting experimental and clinical data on the vasculature density in tumors. Indeed, some studies have demonstrated the validity of using the tumor microvasculature density (MVD) as a prognostic indicator for a wide range of cancers. In addition, quantification of MVD can contribute in assessing the efficacy of antiangiogenic therapies. The quantity MVD is generally expressed as the number of vessels in a 1 mm^2 section, so that denoting by $K\phi_{vasc}$ the vessel volume fraction and by r_{vasc} the mean vessel radius (in mm), we can write

$$\text{MVD} = \frac{K\phi_{vasc}}{\pi r_{vasc}^2}. \tag{51}$$

As expected, the MVD values measured in tumors spread in a rather large interval ranging from about 10 mm^{-2} up to 100 mm^{-2} and more (Kather et al., 2015; Forster et al., 2017).

It is interesting to compute MVD at the final time of our simulation so as to compare its value with experimental data in tumors. According to the simulation, after the tumor invasion the effective vasculature consists of tumor vessels and host arterioles, i.e. $\phi_{vasc} = \phi_v + \phi_z + \phi_{v_a}$, and at 360 days our results give $K\phi_{vasc} = 2.3 \cdot 10^{-2}$. Hence, recalling that in our assumption $r_{vasc} = r_0 + \delta = 1.2 \cdot 10^{-2}$ mm, we get tumor MVD = 50.1 mm^{-2}. Here we are identifying volumetric and surface densities, referring to the ideal case in which vessels are identical and parallel to each other. This is clearly an approximation which however does not alter the order of magnitude.

In the clinical study by Sundfør et al. (1998), both the maximum and the mean vascular density are measured in patients with malignant carcinomas. The mean MVD values are found to range between 10 and 35 mm^{-2} (average 20), whereas the maximum MVD fall in the range 20–70 mm^{-2}. Thus, our simulation result agrees with the higher experimental values. The work by Kather et al. (2015) proposes an automatic approach for vessel counting to make the quantification more objective, accurate and efficient. Mean MVDs measured in prostate tumors range from 48 to 145. So, our result is now close to the lower measured values of MVD. In view of the wide variability of the experimental MVD in tumors, in the paper by Kather et al. (2015), as well as in the review by Forster et al. (2017), the role of MVD as an independent prognostic factor is questioned and the importance of the simultaneous MVD evaluation in normal tissue areas is pointed out.

With the baseline parameters assumed in the simulation, we get a normal tissue MVD = 97.2 mm^{-2} (initial $K\left(\phi_{v_h} + \phi_{v_a}\right)$=0.044), which is approximately double the tumor MVD. This result agrees rather well with the findings reported by Kather et al. (2015) for prostate cancer. We note, however, that other authors have observed tumors which are more vascularized than the healthy tissue. Nevertheless, our result is consistent with the hypothesis of acidic tumor aggression to healthy cells, deriving from a metabolism with less consumption of oxygen and thus requiring a lesser vascularization.

The review by Forster et al. (2017) collects data of studies on head and neck cancers (typically hypoxic) demonstrating that MVD is significantly higher in carcinoma than in the corresponding normal tissue. High concentrations of vascularization are observed in these tumors, which are more commonly associated to high vascular heterogeneity and acute hypoxia. In fact, blood oxygenation levels lower than normal are observed in irregular vascular networks such as the ones of tumors. The data presented by Forster et al. (2017) have mean MVD in healthy tissues in the range 30–88 mm^{-2}, and mean intratumoral MVD correspondingly varying between 58 and 165 mm^{-2}.

To simulate the MVD increase observed in some tumors, we computed the model evolution modifying the proportionality coef-

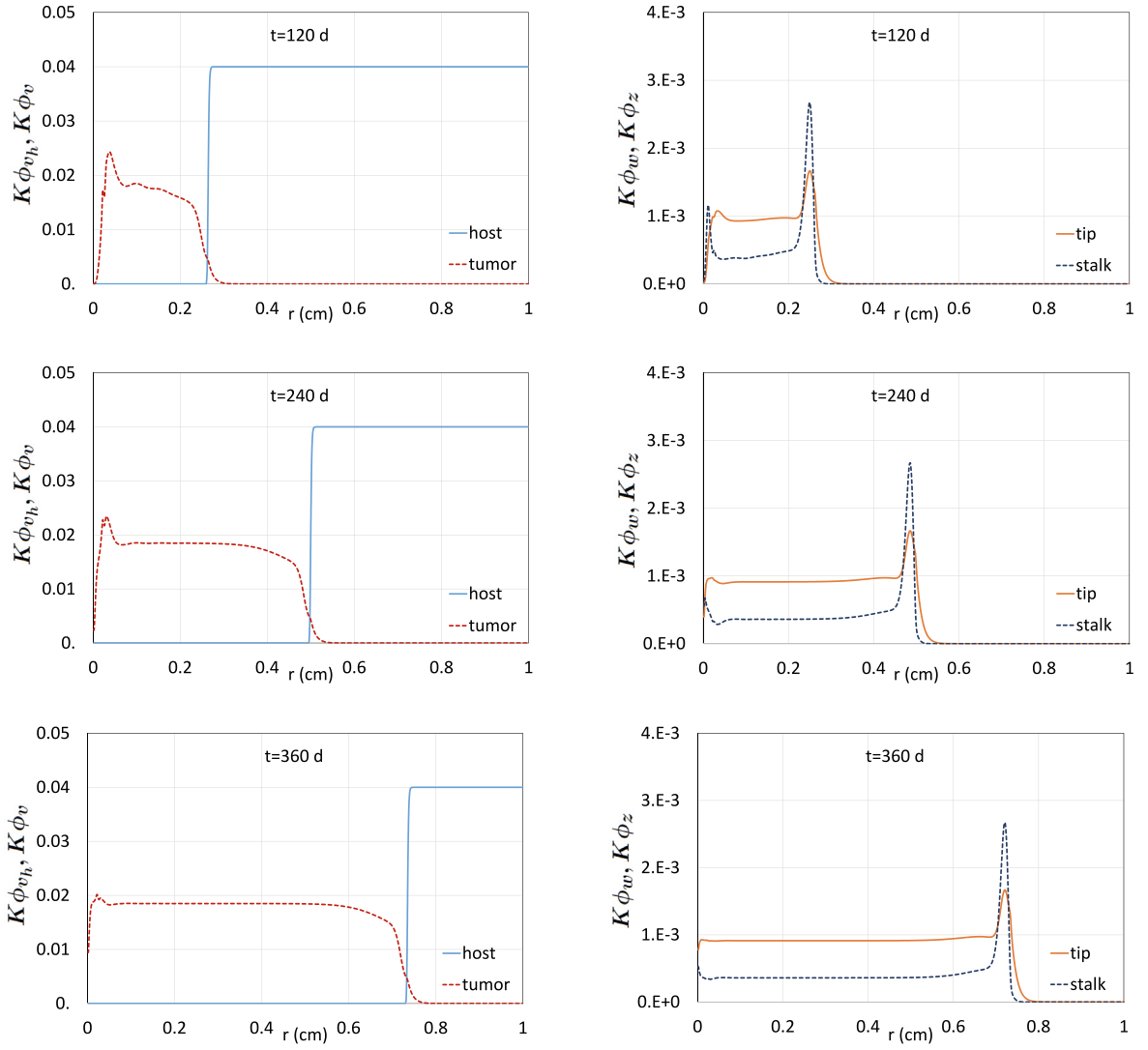

Fig. 3. Simulated evolution of the local volume fractions of vessels. Left panels: $K\phi_{v_h}$ (host, solid line); $K\phi_v$ (tumor, dashed line). Right panels: $K\phi_w$ (sprout tip, solid line); $K\phi_z$ (sprout stalk, solid line).

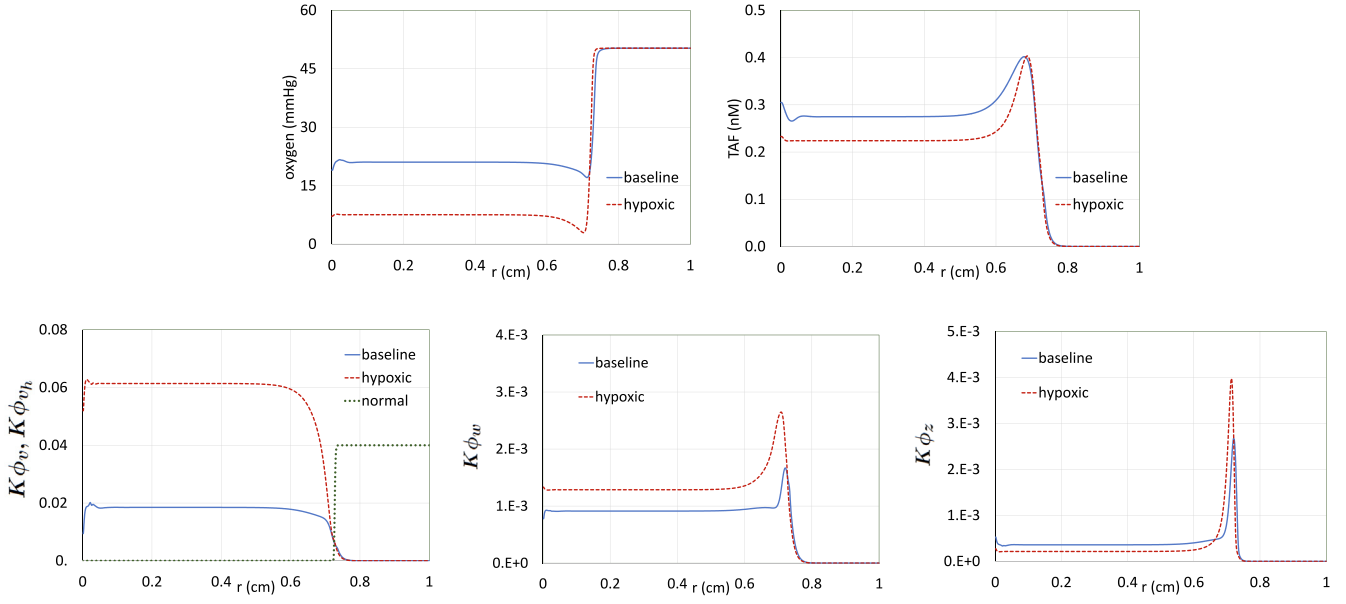

Fig. 4. Comparison of two model evolutions for $t = 360$ days: plot of chemical and vascular quantities with parameter values as in Table 1, with $\gamma_v = \gamma_h$ (baseline, solid line); parameters unchanged except $\gamma_v = 0.1\gamma_h$ (hypoxic, dashed line (tumor vessels), dotted line (normal vessels).

ficients of oxygen supply in Eq. (37), setting $\gamma_v = 0.1\gamma_h$, keeping γ_h and any other parameter to the baseline value of Table 1. The results for $t = 360$ days are shown in Fig. 4 where we also report the baseline plots for comparison. The tumor volume fractions $K\phi_v, K\phi_w, K\phi_z$ are now increased of about three times. In particular, for $r = 0.3$ cm, it is $K\phi_v = 6.1 \cdot 10^{-2}, K\phi_w = 1.3 \cdot 10^{-3}$, $K\phi_z = 2.1 \cdot 10^{-4}$ and, according to (51), we obtain tumor MVD = 143.6 mm^{-2} (normal MVD = 97.2 mm^{-2}). The upper panels of Fig. 4 depicts the oxygen and TAF distributions for the same two simulations. It can be noticed the decrement of the mean oxygen level, which is more than halved in the tumor with $\sigma = 7.64$ mmHg (baseline 21.1 mmHg) and the increment of the TAF gradient near the tumor edge. The obtained curves along with the profiles of $K\phi_w$ and $K\phi_z$ reveal increased tumor vascularity and angiogenesis activity occurring at the margins of the invasive region, as it has experimentally been observed (Forster et al., 2017). The fraction $K\phi_{v_h}$ of normal vessels is displayed for this latter simulation in the bottom left panel of Fig. 4, while the tumor and cell volume fractions are not displayed as they change only negligibly. It can also be noted a slight reduction of the stationary TAF concentration in the hypoxic case, which can be explained by the occurrence of a limited increase in TAF production as compared to the increase in TAF consumption owing to augmented tumor vascularization.

6. Conclusions

Tumors that grow over a size such that the flow of oxygen or nutrients become insufficient to keep cells alive need to develop their own vasculature. They do so by emitting so-called angiogenic factors, which induce sprouting of new vessels from the existing ones and lead them by chemotaxis to the tumor. We have formulated and implemented a model for tumor growth encompassing the phenomenon of angiogenesis. Among the distinctive features of the model we list:

- tumor aggression to healthy cells (in the spirit of Gatenby and Gawlinski, 1996);
- generation and dynamics of the cells giving rise to the new vessels organized in three families (tip cells, sprout cells, tumor vasculature cells);
- detailed derivation of a general family of models of the tumoral angiogenesis-related chemotaxis;
- influence of oxygen concentration on the birth/death rate of tumor cells and of cells involved in the angiogenesis process;
- dynamics of the tumor angiogenic factor;
- crowding effect inhibiting proliferation and cells mobility.

Particular care has been devoted to modeling the motion of tip cells, tracing the way to sprout cells for the construction of the new vasculature. This, indeed, is a fundamental step to understand the growth dynamics of a vascularized tumor. The underlying idea of the proposed family of models of the chemotaxis of the neoplastic vasculature is that tip cell speed is determined by the proliferation rate, while the gradient of the angiogenic factor contributes to select their orientation. The latter is also influenced by a random process which surfaces the chemotactic model as a diffusion component. We think that an appropriate modeling of the chemotaxis driven by the proangiogenic factors is an innovation aimed at arriving to a better understanding of the dynamics of growth of vascularized tumors. Note that the model was derived on a number of biologically driven assumptions reported in the literature (De Smet et al., 2009; Carlier et al., 2012; Phng and Gerhardt, 2009) and not axiomatically proposed.

Numerical simulations carried out in spherical symmetry, starting from a tumor core surrounded by healthy tissue, show that the tumor invasion develops as a traveling wave, progressively replacing the healthy tissue with a vascularized tumor. The theoretical a priori analysis in Appendix A leads to the conclusion that all quantities intervening in the model stay within their expected physical range. The study of nontrivial steady state solution is performed in Appendix B, were we find that in the asymptotic state void of healthy cells all other species must be present. In the final state, deprived of healthy cells, the tumor newly formed vasculature is approximately half of the one formerly present in the healthy tissue, also supported by the survived arteriole, overall providing enough oxygen for the tumor metabolism. Such results are in good agreement with the experimental data, thus indicating that the model is sufficiently flexible to represent also particularly hypoxic tumors characterized by a higher degree of vascularization.

An evident critical aspect of the present model can be recognized in its many biological parameters. Though we strove to retrieve their values from the literature, we eventually had to guess a small number of them based on similarity criteria or by trial and error. However, such parameters do not look particularly critical, in the sense that varying them in a reasonable range does not alter the model outcome by orders of magnitude. This is a clear limitation of the model, but in our opinion it is acceptable for the following reasons. Mathematical models for cancer growth can be roughly divided in two classes: the ones with few, reasonably well known parameters, and the ones, including our model, facing the tough task of dealing with many equations and many parameters. It is well known that cancer is such a complicated disease that normally, when coming to mathematical modeling, authors choose to select just some particular aspects. Simpler models may have the advantage of providing some general answer (like for instance the ones based on ordinary differential equations describing just the growth of the cell population), but as soon as one enters an intrinsically complex process like angiogenesis, there is no way to bypass the difficulty of describing the interplay of several concurrent phenomena. In this case, it is necessary to adopt some compromise and if eventually a good fit is found with experimental results, it means that the model has at least provided a better insight of the problem studied. Of course, this paper is a theoretical biology work. The agreement with experimentally known data may be considered mainly qualitative. We hope that our work could stimulate specific experimental work to assess the relevance of our hypotheses and the realism of our findings. Moreover, the proposed model will be the basis to go a step forward, introducing the action of anti–tumor chemotherapy and of anti–angiogenic drugs. This follow-up work will be the occasion to provide further support by means of a validation based on experimental data.

Moreover, among other future lines of research, it would be of extreme interest (although computationally very challenging) to investigate the impact of the unavoidable extrinsic spatio–temporal stochasticity (ES) (García-Ojalvo and Sancho, 2012) on the dynamics of the proposed system. Indeed: i) it is well known in statistical physics that ES can deeply impact on the dynamics of general traveling waves (Panja, 2004); ii) in non–spatial context some models suggested that ES are of particular interest to better investigate tumor–induced angiogenesis (d'Onofrio and Gandolfi, 2010).

Declaration of Competing Interest

The authors declare that they have no known competing financial interests or personal relationships that could have appeared to influence the work reported in this paper.

Appendix A. Proving that all the model variables are in the physical range

Here, we prove some a priori estimates. Preliminarily, we point out that in the model formulation, all the coefficients depending on the unknown quantities should actually be defined also out of their physical range, since it is not guaranteed a priori that all the unknowns stay in their expected range. We do this tacitly, assuming that the coefficients are extended as constants and in such a way to be continuous. For instance, the function B defined in (1) is extended for $\phi < 0$ and $\phi > \phi^*$ by prolonging B keeping its extreme values constant, so to guarantee its continuity, i.e. $B = 1$ for $\phi < 0$ and $B = 0$ for $\phi > \phi^*$.

Proposition 6.1. Let the system (2), (5), (32)–(36), (37), (39) with boundary conditions (43) have one unique classical solution in the class $\mathscr{C}^{2,1}(\Omega \times (0,T))$. Then all the quantities representing cellular densities are non-negative.

Proof. We can regard Eq. (2) as a linear equation of the form

$$\partial_t n = \boldsymbol{A}n + (B\chi - \mu_n)n, \tag{A.1}$$

where $\boldsymbol{A}$ is a strictly elliptic operator in the divergence form, as long as $B > 0$ (i.e. $\phi < \phi^*$), degenerating when $B = 0$. Though μ_n is strictly positive, the coefficient of n in the last term takes also positive values (if the tumor grows), in principle creating instabilities. However, we may apply the maximum principle in the general form provided by Theorem 2.1 p. 13 of Ladyzenskaja et al. (1968), saying that, even for non-uniformly parabolic equations like (A.1), the estimate $n \geqslant 0$ holds true, since the initial and boundary data taken for n are non-negative. Passing to Eq. (5), setting $M(x,t) = \delta_h n + \mu_h(\sigma)$ we may write

$$h(x,t) = h^0(x) \exp\left(-\int_0^t M(x,\tau)d\tau\right), \tag{A.2}$$

and therefore $h(x,t) = 0$ only at those points where $h_0(x) = 0$, while $0 < h(x,t) \leqslant h_0(x)$ otherwise, for all $t > 0$. In addition, h tends to zero at infinity at all point where n remains strictly positive. Next, the property

$$0 \leqslant v_h(x,t) \leqslant v_h^0(x), \tag{A.3}$$

follows immediately from Eq. (35), remembering that $n \geqslant 0$. Now let us deal with system (32)–(34) with the aim of proving that v, w, and z do not take negative values. We modify Eq. (33) by replacing w by $w_+ = \max(0,w)$, thus defining a new unknown $\tilde{z}$ satisfying

$$\partial_t \tilde{z} = \beta w_+ - k_{an}(v_a + v_h + v + w_+ + \tilde{z})\tilde{z} - \mu_z \tilde{z}. \tag{A.4}$$

Likewise, we modify (34) replacing w by w_+ and z by $\tilde{z}$, thus defining $\tilde{v}$ satisfying

$$\partial_t \tilde{v} = k_{an}(v_a + v_h + w_+ + \tilde{z})(w_+ + \tilde{z}) + k_{an}(w_+ + \tilde{z})\tilde{v} - \mu_v \tilde{v}. \tag{A.5}$$

Returning to (32), we complete the reformulation of the model replacing v, z by $\tilde{v}, \tilde{z}$, respectively, and calling $\tilde{w}$ the new unknown, which is actually the one to be used in (A.4), (A.5). The same changes of variables are to be made when calculating ϕ and in all the remaining equations of the model. At this point we assume that the new model with the same initial and boundary conditions has one unique classical solution, as we made for the original model. Now, looking at (A.4) as a linear differential equation in $\tilde{z}$ (i.e. considering the term $\tilde{z}$ in the brackets as a known function) we deduce that $\tilde{z} \geqslant 0$, and similarly, from (A.5), that $\tilde{v} \geqslant 0$. Finally, the inequality $\tilde{w} \geqslant 0$ follows using the same arguments applied to Eq. (A.1) to prove that $n \geqslant 0$. Therefore $\tilde{w}_+ = \tilde{w}$ and the three equations for the unknowns $\tilde{w}, \tilde{z}, \tilde{v}$ become identical to their original analog. Then the desired result for the triple (w,z,v) is achieved. More precisely, we can say that v and z remain positive in time at all points where they have attained a positive value.It remains to analyze m. It is now ascertained that all the terms at the right hand side of (36), except the last one, are not negative. This is enough to say that m too has the property to stay positive once it has become positive.□

Proposition 6.2. Under the same assumption of Prop. 6.1, we have $0 < \sigma < \sigma_h^*$.

Proof. The proof is obtained by suitably applying the maximum principle to the parabolic Eq. (37).□

Finally, we want to show

Proposition 6.3. Under the same assumptions as above, ϕ never attains the saturation value ϕ^*.

Proof. Let us recall the notation (50) for the local volume fractions of cells and vessels and the consequent expression of the total volume fraction ϕ

$$\phi = \phi_n + \phi_h + \phi_m + K\left(\phi_{v_a} + \phi_{v_h} + \phi_w + \phi_z + \phi_v\right).$$

Multiplying by V_c the model equations for n, h, m, w, z, v, v_h, it is easy to rewrite the model in terms of fractions ϕ_p. Summing up the equations so obtained and recalling that ϕ_a is assumed constant, we formally get the following expression of $\partial_t \phi$:

$$\begin{aligned} \partial_t \phi = \;& \nabla \cdot (D_n B(\phi) \nabla \phi_n) + B(\phi)\chi(\sigma)\phi_n + K\alpha(\psi,\phi)\left(\phi_{v_h} + \phi_v\right) \\ +\; & K\nabla \cdot (D_w(\psi,\phi)\nabla\phi_w) - K\nabla \cdot \left(u_{tip}(\psi,\phi) q(|\nabla\psi|)\tfrac{\nabla\psi}{|\nabla\psi|}\phi_w\right) \\ & + K\beta(\psi,\phi)\phi_w \\ +\; & (1-K)\left(\mu_w\phi_w + \mu_z\phi_z + \mu_v\phi_v + \tfrac{\delta_{v_h}}{V_c}\phi_n\phi_{v_h}\right) - \lambda_m\phi_m. \end{aligned} \tag{A.6}$$

We have seen that, if the system (2), (5), (32)–(36), (37), (39) with boundary conditions (43) has a unique solution with $\mathscr{C}^{2,1}$ components then all cells concentrations are non-negative. Along such a solution, it is obviously $\phi(x,t) \geqslant 0$ and we prove by contradiction that $\phi(x,t) < \phi^*$ holds.

To this end, let us suppose that there exists a time $\bar{t} > 0$ such that ϕ attains the value ϕ^* for the first time in $\bar{t}$, and let $\omega^* \subset \Omega$ be the set of points $\bar{x}$ such that $\phi(\bar{x},\bar{t}) = \phi^*$. It is easily seen that ϕ is constant on the boundary of Ω, where there is no evolution of cells concentration, thus $\omega*$ does not include points of $\partial\Omega$. Since $\phi(x,0) < \phi^*$ for any x, the value ϕ^* is necessarily reached from below.

Therefore the points $\bar{x} \in \omega^*$ are maximum points for $\phi(\cdot,\bar{t})$, so that $\nabla\phi = 0$ in $(\bar{x},\bar{t})$. In addition, it is $B(\phi(\bar{x},\bar{t})) = 0$, which implies that the functions α, β, u_{tip}, and D_w are also null in $(\bar{x},\bar{t})$. So, taking into account that the solution is assumed to have bounded spatial derivatives up to the second order, Eq. (6) in $(\bar{x},\bar{t})$ reduces to

$$\begin{aligned} \partial_t\phi(\bar{x},\bar{t}) = (1-K)\left(\mu_w\phi_w(\bar{x},\bar{t}) + \mu_z\phi_z(\bar{x},\bar{t}) + \mu_v\phi_v(\bar{x},\bar{t}) + \frac{\delta_{v_h}}{V_c}\phi_n(\bar{x},\bar{t})\phi_{v_h}(\bar{x},\bar{t})\right) \\ - \lambda_m\phi_m(\bar{x},\bar{t}). \end{aligned} \tag{A.7}$$

The first term of the r.h.s. of Eq. (7) is non positive since $K > 1$. On the other hand, we can prove that $m(x,t)$ is strictly positive for any $(x,t), t > 0$ and $x \in \Omega$. Indeed, from (36) and (4) we deduce

$$\partial_t m \geqslant \mu_0 n - \lambda_m m. \tag{A.8}$$

Furthermore, as proved Prop. 6.1, it is $n(x,t) > 0$ for $0 < t < \bar{t}$ and $x \in \Omega$. Thus, from (8) and in view of the comparison theorem, we

have $m(\bar{x},\bar{t}) > 0$. As a consequence, $\partial_t \phi(\bar{x},\bar{t})$ is negative, which leads to a contradiction. Therefore, for any solution such that $\phi(x,0) < \phi^*$, we have $\phi(x,t) < \phi^*$ for any $t \in (0,T]$ and $x \in \Omega$. We remark that the inequality just obtained implies an obvious upper bound for all cells concentrations. □

Appendix B. Steady state solutions with tumor cells only

Here we investigate the asymptotic state in which no healthy cells are left, namely $h = 0, v_h = 0$, which are consequences of (5) and (35), respectively. Eq. (2) provides

$$B(\phi)\chi(\sigma) - \mu_n(\sigma) = 0, \tag{B.1}$$

expressing ϕ as a function of σ, provided that the parameters are correctly prescribed. We recall that if σ is in a suitable range then the loss term $\mu_n(\sigma)$ equals μ_0. From Eq. (B.1), being $B(\phi)$ a monotonically decreasing function of ϕ, we derive a unique solution for ϕ. We deduce that asymptotically $\phi < \phi*$. From Eq. (37), we get the following asymptotic value of the ratio n/v as a function of σ:

$$n = \gamma_v v(\sigma_v^* - \sigma)/H_n(\sigma), \tag{B.2}$$

which requires $\sigma < \sigma_v^*$. Next we consider the asymptotic form of Eqs. (32)–(34). Remembering that $\beta = c\alpha$, we have

$$\alpha v = (X + \mu_w)w, \quad \text{or } \frac{v}{w} = \frac{X+\mu_w}{\alpha}, \tag{B.3}$$

$$c\alpha w = (X + \mu_z)z, \quad \text{or } \frac{z}{w} = \frac{c\alpha}{X+\mu_z}, \tag{B.4}$$

$$\mu_v v = X(w + z), \tag{B.5}$$

where we have set $X = \kappa_{an}(v_a + \eta)$ and

$$\eta = v + z + w. \tag{B.6}$$

Dividing (B.5) by w and using (B.3), (B.4) we get the following quadratic equation:

$$\left(1 - \frac{\mu_v}{\alpha}\right)X^2 + \left(\mu_z + c\alpha - \frac{\mu_v\mu_w + \mu_v\mu_z}{\alpha}\right)X - \frac{\mu_v\mu_w\mu_z}{\alpha} = 0, \tag{B.7}$$

from which we can find X, and consequently η, in terms of α. For the moment, we consider α as a parameter. We know that it is a function of ψ and of σ (through Eq. (9)). The analysis of (B.7) is not trivial. For instance, if we take $\mu_w = \mu_z = \mu$ and we set $\alpha = \mu_v/\theta$, (B.7) reduces to

$$(1-\theta)X^2 + \left[\mu(1-2\theta) + \frac{c}{\theta}\right]X - \theta\mu^2 = 0,$$

whose discriminant can be written in the form $(\mu + c/\theta)^2 - 4\mu(2\mu\theta + c)$, which requires θ small enough to be positive. This can be checked only a posteriori, once we determine α. Now, we solve the linear system (B.3), (B.4), (B.6) finding

$$v = \frac{1}{\Delta}\eta(X+\mu_w)(X+\mu_z), \tag{B.8}$$

$$w = \frac{1}{\Delta}\alpha\eta(X+\mu_z), \tag{B.9}$$

$$z = \frac{1}{\Delta}c\alpha^2\eta, \tag{B.10}$$

where $\Delta = \alpha[c\alpha + (X+\mu_z)] + (X+\mu_w)(X+\mu_z)$. Thus, we have expressed implicitly v, w, z in terms of α. The dependence of n on α and σ is emphasized by (B.2). Now we shift our attention to ψ, i.e. to P, considering the steady state of Eq. (9))

$$\pi_P(\sigma)n = C_P(P)\eta + \lambda_P P(\phi_P^* - \phi), \tag{B.11}$$

which provides P, and hence ψ, as a function of σ and α, keeping into account what we have found so far. Note that the r.h.s. of (B.11) grows monotonically from 0 to ∞ as P runs from 0 to ∞ guaranteeing the existence of a solution. Now we have reached the conclusion $\alpha = \alpha(\sigma)$, defined implicitly through (9). Concerning dead cells, from (36) we have

$$\lambda_m m = \mu_n(\sigma)n + \mu_v v + \mu_w w + \mu_z z. \tag{B.12}$$

Thus, m is a function of σ too. Finally, we pass to (42), which we write in the form

$$\phi = V_c(n + m + K(v_a + \eta)), \tag{B.13}$$

and which has the role of determining σ, since the two sides of the equation have been found independently as functions of σ. Of course, all the steps above are feasible if the parameters are given in a suitable way.

References

Adair, T.H., Montani, J.P., 2010. Angiogenesis. Morgan Claypool Life Sci.

Anderson, A., Chaplain, M., Reimbert, C., Vargas, C.A., 2000. A gradient-driven mathematical model of antiangiogenesis. Math. Comput. Model 32, 1141–1152.

Anderson, A.R.A., Chaplain, M.A.J., 1998. Continuous and discrete mathematical models of tumor-induced angiogenesis. Bull. Math. Biol. 60, 857–899.

Ariza de Schellenberger, A., Bergs, J., Sack, I., Taupitz, M., 2018. The Extracellular Matrix as a Target for Biophysical and Molecular Magnetic Resonance Imaging. Springer International Publishing, Cham, pp. 123–150.

Ausprunk, D.H., Folkman, J., 1977. Migration and proliferation of endothelial cells in preformed and newly formed blood vessels during tumor angiogenesis. Microvasc. Res. 14, 53–65.

Balding, D., McElwain, D.L., 1985. A mathematical model of tumour-induced capillary growth. J. Theor. Biol. 114, 53–73.

Bellomo, N., Bellouquid, A., Nieto, J., Soler, J., 2013. Modeling chemotaxis from l^2-closure moments in kinetic theory of active particles. Discr. Cont. Dyn. Syst. – B 18, 847–863.

Bertuzzi, A., d'Onofrio, A., Fasano, A., Gandolfi, A., 2003. Regression and regrowth of tumour cords following single-dose anticancer treatment. Bull. Math. Biol. 65, 903–931.

Bertuzzi, A., Bruni, C., Fasano, A., Gandolfi, A., Papa, F., Sinisgalli, C., 2010. Response of tumor spheroids to radiation: modeling and parameter estimation. Bull. Math. Biol. 72, 1069–1091.

Bertuzzi, A., Fasano, A., Gandolfi, A., Sinisgalli, C., 2010. Necrotic core in EMT6/Ro tumour spheroids: is it caused by an ATP deficit? J. Theor. Biol. 262, 142–150.

Bruehlmeier, M., Roelcke, U., Bläuenstein, P., Missimer, J., Schubiger, P.A., Locher, J. T., Pellikka, R., Ametamey, S.M., 2003. Measurement of the extracellular space in brain tumors using 76br-bromide and PET. J. Nucl. Med. 44, 1210–1218.

Buckley, D.L., Bui, J.D., Phillips, M.I., Blackband, S.J., 1999. MRI measurement of cell volume fraction in the perfused rat hippocampal slice. Magn. Reson. Med. 42, 603–607.

Carlier, A., Geris, L., Bentley, K., Carmeliet, G., Carmeliet, P., Van Oosterwyck, H., 2012. MOSAIC: a multiscale model of osteogenesis and sprouting angiogenesis with lateral inhibition of endothelial cells. PLoS Comput. Biol. 8, e1002724.

Carmeliet, P., Jain, R.K., 2011. Molecular mechanisms and clinical applications of angiogenesis. Nature 473, 298–307.

Casciari, J.J., Sotirchos, S.V., Sutherland, R.M., 1992. Mathematical modelling of microenvironment and growth in EMT6/Ro multicellular tumour spheroids. Cell Prolif. 25, 1–22.

Chaplain, M.A., Stuart, A.M., 1993. A model mechanism for the chemotactic response of endothelial cells to tumour angiogenesis factor. IMA J. Math. Appl. Med. Biol. 10, 149–168.

Chaplain, M.A.J., McDougall, S.R., Anderson, A.R.A., 2006. Mathematical modeling of tumor-induced angiogenesis. Annu. Rev. Biomed. Eng. 8, 233–257.

Darzynkiewicz, Z., Juan, G., Li, X., Gorczyca, W., Murakami, T., Traganos, F., 1997. Cytometry in cell necrobiology: analysis of apoptosis and accidental cell death (necrosis). Cytometry 27, 1–20.

De Smet, F., Segura, I., De Bock, K., Hohensinner, P.J., Carmeliet, P., 2009. Mechanisms of vessel branching: filopodia on endothelial tip cells lead the way. Arterioscler. Thromb. Vasc. Biol. 29, 639–649.

Donahue, K.M., Weisskoff, R.M., Parmelee, D.J., Callahan, R.J., Wilkinson, R.A., Mandeville, J.B., Rosen, B.R., 1995. Dynamic Gd-DTPA enhanced MRI measurement of tissue cell volume fraction. Magn. Reson. Med. 34, 423–432.

Donnem, T., Hu, J., Ferguson, M., Adighibe, O., Snell, C., Harris, A.L., Gatter, K.C., Pezzella, F., 2013. Vessel co-option in primary human tumors and metastases: an obstacle to effective anti-angiogenic treatment?. Cancer Med. 2, 427–436.

d'Onofrio, A., Gandolfi, A., 1999. Tumour eradication by antiangiogenic therapy: analysis and extensions of the model by Hahnfeldt et al. (1999). Math. Biosci. 191 (2), 159–184.

d'Onofrio, A., Gandolfi, A., 2006. The response to antiangiogenic anticancer drugs that inhibit endothelial cell proliferation. Appl. Math. Comput. 181, 1155–1162.

d'Onofrio, A., Gandolfi, A., 2009. A family of models of angiogenesis and anti-angiogenesis anti-cancer therapy. Math. Med. Biol. 26, 63–95.

d'Onofrio, A., Gandolfi, A., 2010. Chemotherapy of vascularised tumours: role of vessel density and the effect of vascular "pruning". J. Theor. Biol. 264 (2), 253–265.

d'Onofrio, A., Gandolfi, A., 2010. Resistance to antitumor chemotherapy due to bounded-noise-induced transitions. Phys. Rev. E 82, (6) 061901.
d'Onofrio, A., Gandolfi, A., Rocca, A., 2009. The dynamics of tumour-vasculature interaction suggests low-dose, time-dense anti-angiogenic schedulings. Cell Prolif. 42, 317–329.
Fasano, A., Herrero, M.A., Rocha Rodrigo, M., 2009. Slow and fast invasion waves in a model of acid-mediated tumour growth. Math. Biosci. 220, 45–56.
Forster, J.C., Harriss-Phillips, W.M., Douglass, M.J., Bezak, E., 2017. A review of the development of tumor vasculature and its effects on the tumor microenvironment. Hypoxia 5, 21–32.
Franko, A., Sutherland, R.M., 1978. Rate of death of hypoxic cells in multicell spheroids. Radiat. Res. 76, 561–572.
Freyer, J.P., Sutherland, R.M., 1985. A reduction in the in situ rates of oxygen and glucose consumption of cells in EMT6/Ro spheroids during growth. J. Cell Physiol. 124, 516–524.
Freyer, J.P., Sutherland, R.M., 1986. Regulation of growth saturation and development of necrosis in EMT6/Ro multicellular spheroids by the glucose and oxygen supply. Cancer Res. 46, 3504–3512.
García-Ojalvo, J., Sancho, J., 2012. Noise in spatially extended systems. Springer Science & Business Media.
Gatenby, R.A., Gawlinski, E.T., 1996. A reaction-diffusion model of cancer invasion. Cancer Res. 56, 5745–5753.
Gatenby, R.A., Gawlinski, E.T., 2003. The glycolytic phenotype in carcinogenesis and tumor invasion: insights through mathematical models. Cancer Res. 63, 3847–3854.
Gerhardt, H., Golding, M., Fruttiger, M., Ruhrberg, C., Lundkvist, A., Abramsson, A., Jeltsch, M., Mitchell, C., Alitalo, K., Shima, D., Betsholtz, C., 2003. VEGF guides angiogenic sprouting utilizing endothelial tip cell filopodia. J. Cell Biol. 161, 1163–1177.
Geudens, I., Gerhardt, H., 2011. Coordinating cell behaviour during blood vessel formation. Development 138, 4569–4583.
Hahnfeldt, P., Panigrahy, D., Folkman, J., Hlatky, L., 1999. Tumor development under angiogenic signaling: a dynamical theory of tumor growth, treatment response, and postvascular dormancy. Cancer Res. 59 (19), 4770–4775.
Hashimoto, K., Murakami, T., Dono, K., Hori, M., Kim, T., et al., 2006. Assessment of the severity of liver disease and fibrotic change: the usefulness of hepatic CT perfusion imaging. Oncol. Rep. 16, 677–683.
Hillen, T., 2004. On the l2-moment closure of transport equations: the Cattaneo approximation. Discr. Cont. Dyn. Syst. – B 4, 961–982.
Hillen, T., 2005. On the l2-moment closure of transport equations: the general case. Discr. Cont. Dyn. Syst. – B 5, 299–318.
Hillen, T., Painter, K.J., 2009. A user's guide to PDE models for chemotaxis. J. Math. Biol. 58, 183–217.
Ito, H., Kanno, I., Iida, H., Hatazawa, J., Shimosegawa, E., Tamura, H., Okudera, T., 2001. Arterial fraction of cerebral blood volume in humans measured by positron emission tomography. Ann. Nucl. Med. 15, 111–116.
Kather, J.N., Marx, A., Reyes-Aldasoro, C.C., Schad, L.R., Zöllner, F.G., Weis, C., 2015. Continuous representation of tumor microvessel density and detection of angiogenic hotspots in histological whole-slide images. Oncotarget 6, 19163–19176.
Keller, E.F., Segel, L.A., 1971. Model for chemotaxis. J. Theor. Biol. 30, 225–234.
Krol, A., Maresca, J., Dewhirst, M.W., Yuan, F., 1999. Available volume fraction of macromolecules in the extravascular space of a fibrosarcoma: implications for drug delivery. Cancer Res. 59, 4136–4141.
Krüger-Genge, A., Blocki, A., Franke, R.P., Jung, F., 2019. Vascular endothelial cell biology: an update. Int. J. Mol. Sci. 20, 4411. https://doi.org/10.3390/ijms20184411.
Ladyzenskaja, O.A., Solonnikov, V.A., Uralceva, N.N., 1968. Linear and quasilinear equations of parabolic type. AMS Transl. Math., Monographs 27.
Lai, N., Zhou, H., Saidel, G.M., Wolf, M., McCully, K., Gladden, L.B., Cabrera, M.E., 2009. Modeling oxygenation in venous blood and skeletal muscle in response to exercise using near-infrared spectroscopy. J. Appl. Physiol. 106, 1858–1874.
Ledzewicz, Urszula, Schättler, Heinz, 2012. Multi-input optimal control problems for combined tumor anti-angiogenic and radiotherapy treatments. J. Optim. Theory Appl. 153 (1), 195–224.
Levine, H., Rappel, W.J., 2013. The physics of eukaryotic chemotaxis. Phys. Today 66, 24–30.
Mac Gabhann, F., Popel, A.S., 2004. Model of competitive binding of vascular endothelial growth factor and placental growth factor to VEGF receptors on endothelial cells. Am. J. Physiol. Heart Circ. Physiol. 286, 153–164.
Maisonpierre, P.C., Suri, C., Jones, P.F., Bartunkova, S., Wiegand, S.J., Radziejewski, C., Compton, D., McClain, J., Aldrich, T.H., Papadopoulos, N., Daly, T.J., Davis, S., Sato, T.N., Yancopoulos, G.D., 1997. Angiopoietin-2, a natural antagonist for Tie2 that disrupts in vivo angiogenesis. Science 277, 55–60.
Mantzaris, N., Webb, S., Othmer, H., 2004. Mathematical modeling of tumor-induced angiogenesis. J. Math. Biol. 49, 111–187.
Nagy, J.A., Chang, S.H., Dvorak, A.M., Dvorak, H.F., 2009. Why are tumour blood vessels abnormal and why is it important to know?. Br. J. Cancer 100, 865–869.
Othmer, H.G., Dunbar, S.R., Alt, W., 1988. Models of dispersal in biological systems. J. Math. Biol. 26, 263–298.
Panja, D., 2004. Effects of fluctuations on propagating fronts. Phys. Rep. 393, 87–174.
Patlak, C.S., 1953. Random walk with persistence and external bias. Bull. Math. Biol. 15, 311–338.
Perles-Barbacaru, A.T., van der Sanden, B.P., Farion, R., Lahrech, H., 2012. How stereological analysis of vascular morphology can quantify the blood volume fraction as a marker for tumor vasculature: comparison with magnetic resonance imaging. J. Cereb. Blood Flow Metab. 32, 489–501.
Perthame, B., 2004. PDE models for chemotactic movements: parabolic, hyperbolic and kinetic. Appl. Math. 49, 539–564.
Phng, L.K., Gerhardt, H., 2009. Angiogenesis: a team effort coordinated by notch. Dev. Cell 16, 168–208.
Rivero, M.A., Tranquillo, R.T., Buettner, H.M., Lauffenburger, D.A., 1989. Transport models for chemotactic cell populations based on individual cell behavior. Chem. Eng. Sci. 44, 2881–2897.
Scianna, M., Bell, C.G., Preziosi, L., 2013. A review of mathematical models for the formation of vascular networks. J. Theor. Biol. 333, 174–209.
Serini, G., Ambrosi, D., Giraudo, E., Gamba, A., Preziosi, L., Bussolino, F., 2003. Modeling the early stages of vascular network assembly. EMBO J. 22 (8), 1771–1779.
Stamper, I.J., Owen, M.R., Maini, P.K., Byrne, H.M., 2010. Oscillatory dynamics in a model of vascular tumour growth-implications for chemotherapy. Biol. Direct 5. https://doi.org/10.1186/1745-6150-5-27.
Stroock, D.W., 1974. Some stochastic processes which arise from a model of the motion of a bacterium. Probab. Theor. Relat. Field 28, 305–315.
Sun, S., Wheeler, M.F., Obeyesekere, M., Patrick Jr, C.W., 2005. A deterministic model of growth factor-induced angiogenesis. Bull. Math. Biol. 67, 313–337.
Sundfør, K., Lyng, H., Rofstad, E.K., 1998. Tumour hypoxia and vascular density as predictors of metastasis in squamous cell carcinoma of the uterine cervix. Br. J. Cancer 78, 822–827.
Swanson, K.R., Rockne, R.C., Claridge, J., Chaplain, M.A., Alvord Jr, E.C., Anderson, A. R., 2011. Quantifying the role of angiogenesis in malignant progression of gliomas: in silico modeling integrates imaging and histology. Cancer Res. 71, 7366–7375.
Tranquillo, R.T., Lauffenburger, D.A., Zigmond, S.H., 1988. A stochastic model for leukocyte random motility and chemotaxis based on receptor binding fluctuations. J. Cell Biol. 106, 303–309.
Travasso, R.D., Corvera Poiré, E., Castro, M., Rodriguez-Manzaneque, J.C., Hernàndez-Machado, A., 2011. Tumor angiogenesis and vascular patterning: a mathematical model. PLoS One 6, e19989.
Tsyganov, M.A., Brindley, J., Holden, A.V., Biktashev, V.N., 2004. Soliton-like phenomena in one-dimensional cross-diffusion systems: a predator-prey pursuit and evasion example. Physica D 197, 18–33.
Vaupel, P., Kallinowski, F., Okunieff, P., 1989. Blood flow, oxygen and nutrient supply, and metabolic microenvironment of human tumors: a review. Cancer Res. 49, 6449–6465.
Vaupel, P., Schlenger, K., Knoop, C., Höckel, M., 1991. Oxygenation of human humors: evaluation of tissue oxygen distribution in breast cancers by computerized O2 tension measurements. Canc Res. 51, 3316–3322.
Voutouri, C., Kirkpatrick, N.D., Chung, E., Mpekris, F., Baish, J.W., Munn, L.L., Fukumura, D., Stylianopoulos, T., Jain, R.K., 2019. Experimental and computational analyses reveal dynamics of tumor vessel cooption and optimal treatment strategies. Proc. Natl. Acad. Sci. 116 (7), 2662–2671.
Welter, M., Bartha, K., Rieger, H., 2008. Emergent vascular network inhomogeneities and resulting blood flow patterns in a growing tumor. J. Theor. Biol. 250, 257–280.
Zigmond, S.H., 1977. Ability of polymorphonuclear leukocytes to orient in gradients of chemotactic factors. J. Cell Biol. 75, 606–616.